

**A STUDY OF OPTICAL AND PHYSICAL PROBE DIAGNOSTIC TECHNIQUES  
FOR ATMOSPHERIC-PRESSURE PLASMAS**

**by**

**STEVEN J. DOYLE**

**A THESIS**

**Submitted in partial fulfillment of the requirements  
for the degree of Master of Science in Engineering  
in  
The Department of Mechanical and Aerospace Engineering  
to  
The School of Graduate Studies  
of  
The University of Alabama in Huntsville**

**HUNTSVILLE, ALABAMA**

**2017**

In presenting this thesis in partial fulfillment of the requirements for a master's degree from The University of Alabama in Huntsville, I agree that the library of this University shall make it freely available for inspection. I further agree that permission for extensive copying for scholarly purposes may be granted by my advisor or, in his/her absence, by the Chair of the Department or the Dean of the School of Graduate Studies. It is also understood that due recognition shall be given to me and to The University of Alabama in Huntsville in any scholarly use which may be made of any material in this thesis.

---

Steven J. Doyle

---

Date



## ABSTRACT

The School of Graduate Studies  
The University of Alabama in Huntsville

Degree Master of Science College/Dept. Engineering/Mechanical and  
in Engineering Aerospace Engineering  
Name of Candidate Steven J. Doyle  
Title A Study of Optical and Physical Probe Diagnostic Techniques for  
Atmospheric-Pressure Plasmas

This study investigated the application of physical probes and optical emission spectroscopy to an atmospheric microplasma jet to determine the gas temperature, electron temperature, and electron density of the plasma. Emission lines and species of interest were chosen to determine the impact of experimental configuration on the accuracy of measurements. The results showed that there is a noticeable difference in not only each of the different gas temperature determination methods, but also for individual argon spectral lines when using van der Waals broadening. The usefulness of argon spectral lines also appears to vary with electrode configurations and temperatures. Electron temperature and density were found to increase and decrease, respectively, with an increase in measurement distance. These effects may be attributed to high collisionality via neutralization collisions and continuum flow turbulence due to mixing with ambient air.

Abstract Approval: Committee Chair \_\_\_\_\_  
Dr. Kunning G. Xu

Department Chair \_\_\_\_\_  
Dr. Keith Hollingsworth

Graduate Dean \_\_\_\_\_  
Dr. David Berkowitz

## ACKNOWLEDGEMENTS

I would like to thank my advisor, Dr. Kunning Xu, for giving me the opportunity to pursue research in the Plasma and Electrodynamics Research Lab at the Propulsion Research Center. Without his continual support and guidance, this work would not have been possible. As one of his students, I have not only become a better engineering, but also a better researcher.

I would also like to thank the Propulsion Research Center Lab Supervisor Dr. David Lineberry and Facility Engineer Tony Hall, who were always willing to answer any question I had. Their feedback on experimental setups, analysis, and safety were vital for the success of this work.

Credit is also due to my fellow colleagues at the Plasma and Electrodynamics Research Lab. I am grateful for the assistance of Roberto Dextre, Paulo Salvador, Ethan Hopping, Ryan Gott, Bradley Henderson, and Noah Latham with experimental setup and testing.

Finally, I would like to thank my parents for their continuous love and support. Being away from New Jersey for the last six years was no easy task. They pushed me to give my best effort and make the most out of my time at UAH.

## TABLE OF CONTENTS

<b>LIST OF FIGURES.....</b>	<b>viii</b>
<b>LIST OF TABLES.....</b>	<b>x</b>
<b>LIST OF SYMBOLS.....</b>	<b>xi</b>
<b>1. CHAPTER 1 INTRODUCTION .....</b>	<b>2</b>
1.1 Problem Statement .....	3
1.2 Research Contributions .....	5
<b>2. CHAPTER 2 BACKGROUND .....</b>	<b>7</b>
<b>2.1 Atmospheric Microplasma Configurations .....</b>	<b>7</b>
<b>2.2 Review of Literature .....</b>	<b>9</b>
2.2.1 Spectral Line Broadening Mechanisms .....	9
2.2.2 Gas Temperature Determination from van der Waals Broadening .....	10
2.2.3 Gas Temperature Determination from OH and N <sub>2</sub> .....	15
2.2.4 Electron Properties from Stark Broadening of Hydrogen.....	20
2.2.5 Langmuir Probes .....	22
<b>3. CHAPTER 3 EXPERIMENTAL METHODS .....</b>	<b>24</b>
<b>3.1 Experimental Setup .....</b>	<b>24</b>
3.1.1 AMPJ Electrode Configurations .....	27
3.1.2 Spectra Analysis Software .....	28
3.1.3 Langmuir Probes .....	28
<b>3.2 Diagnostic Theory .....</b>	<b>30</b>
3.2.1 Optical Emission Spectroscopy Spectral Line Shape .....	30
3.2.2 Boltzmann Plot.....	37
3.2.3 Hydrogen Cross Point Method.....	37
3.2.4 Langmuir Probe Theory .....	38
<b>4. CHAPTER 4 RESULTS .....</b>	<b>43</b>
<b>4.1 Gas Temperature Determination .....</b>	<b>43</b>

4.1.1	Comparison of Argon Broadening Components.....	43
4.1.2	OH (A-X) Spectra.....	45
4.1.3	N <sub>2</sub> (C-B) Spectra.....	49
4.1.4	van der Waals Calculations of Argon (2p-1s).....	50
4.1.5	Thermocouples.....	53
4.1.6	Method Comparison.....	53
<b>4.2</b>	<b>Electron Temperature and Electron Density Determination .....</b>	<b>55</b>
4.2.1	Electron Temperature.....	56
4.2.2	Electron Density and SLP Regimes.....	58
<b>5.</b>	<b>CHAPTER 5 DISCUSSION.....</b>	<b>62</b>
<b>5.1</b>	<b>Gas Temperature .....</b>	<b>62</b>
<b>5.2</b>	<b>Electron Temperature and Density .....</b>	<b>66</b>
<b>5.3</b>	<b>Comparison to Literature .....</b>	<b>70</b>
<b>6.</b>	<b>CHAPTER 6 CONCLUSION .....</b>	<b>73</b>
<b>6.1</b>	<b>Gas Temperature .....</b>	<b>73</b>
<b>6.2</b>	<b>Electron Temperature and Electron Density .....</b>	<b>74</b>
<b>6.3</b>	<b>Future Work.....</b>	<b>75</b>
<b>APPENDIX A</b>	<b>.....</b>	<b>77</b>
<b>APPENDIX B</b>	<b>.....</b>	<b>78</b>
<b>APPENDIX C</b>	<b>.....</b>	<b>80</b>
<b>APPENDIX D</b>	<b>.....</b>	<b>84</b>
<b>REFERENCES</b>	<b>.....</b>	<b>86</b>

## LIST OF FIGURES

FIGURE	PAGE
2.1 Schematics of DBD-like plasma jets.....	8
2.2 Schematics of DBD plasma jets.....	8
2.3 OH (A-X) simulated spectrum using Specair.....	16
2.4 N <sub>2</sub> (C-B) simulated spectrum using Specair.....	17
3.1 Diagram of complete experimental setup.....	24
3.2 Experimental setup schematic.....	25
3.3 AMPJ picture.....	25
3.4 Adhesive thermocouple.....	26
3.5 Linear-field wiring diagram.....	27
3.6 Cross-field wiring diagram.....	28
3.7 Probe locations in the plasma.....	29
3.8 Example of single Langmuir probe.....	29
3.9 Relevant fit profiles.....	31
3.10 He-Ne laser emission spectra.....	34
3.11 Flowing plasma regimes.....	40
4.1 OH (A-X) emission spectrum at 50 W, linear-field configuration.....	45
4.2 OH (A-X) gas temperature results.....	47
4.3 Specair simulation results at 50 W, linear-field configuration.....	47
4.4 Lifbase Simulation results at 50 W, linear-field configuration.....	48
4.5 N <sub>2</sub> (C-B) emission spectrum at 70 W, linear-field configuration.....	49
4.6 N <sub>2</sub> (C-B) gas temperature results, linear-field configuration.....	50
4.7 Argon spectra lines at 50 W, linear-field configuration.....	51

4.8	Van der Waals broadening results, linear-field configuration.....	52
4.9	Van der Waals broadening results, cross-field configuration.....	52
4.10	Thermocouple results.....	53
4.11	Temperature results for linear-field and cross-field jet.....	55
4.12	DLP I-V plots at 70 W, various distances.....	56
4.13	DLP I-V plots at 5 mm, various powers.....	56
4.14	Comparison between raw and smoothed DLP data.....	57
4.15	Electron temperature as function of distance, 50-90 W.....	58
4.16	Flowing plasma regimes as a function of probe location, 70 W.....	59
4.17	Plasma densities as a function of distance, 50-90 W.....	61
5.1	Doppler and van der Waals broadening values as a function of temperature, 738 nm.....	63
5.2	Sample Boltzmann plots for OH (A-X) and N <sub>2</sub> (C-B) .....	65
5.3	Sample comparison of experimental and simulated OH (A-X) spectra.....	65
5.4	Example of DLP data for 70 W.....	67
5.5	Sample spectra for hydrogen species.....	70

## LIST OF TABLES

<b>TABLE</b>	<b>PAGE</b>
2.1 Common argon spectral lines and transitions.....	11
3.1 Plasma density solutions for high-pressure Langmuir probe regimes.....	41
4.1 Broadening parameter values at $T_e = 3.45$ eV, $n_e = 2.5 \times 10^{12}$ cm <sup>-3</sup> .....	45
4.2 Probe regime criteria values at -145 V.....	60
A.1 Argon line transition probabilities and energies.....	77
B.1 Boltzmann plot spectra information.....	78
B.2 Boltzmann plot calculations for linear-field OH (A-X) spectra.....	79
B.3 Boltzmann plot calculations for cross-field OH (A-X) spectra.....	79

## LIST OF SYMBOLS

### SYMBOL

$A$	Transition probability
$a_0$	Bohr radius
$c$	Speed of light
$D$	Smallest characteristic dimension
$E$	Energy of level
$E_{ion}^H$	Hydrogen ionization energy
$G$	Gauss
$h$	Planck's constant
$I_{i,sat}$	Ion current saturation
$k$	Boltzmann's constant
$L$	Lorentzian
$l$	Orbital quantum number
$M$	Atomic mass
$N$	Number density
$n$	Perturber density
$n^{*2}$	Effective quantum number
$n_0$	Plasma Density
$N_e$	Electron density
$p$	Pressure
$R^2$	Squared radius of the emitting atom
$Re$	Electric Reynolds number
$r_p$	Probe radius

$r_{sheath}$	Sheath radius
$T$	Gas temperature
$T_e$	Electron temperature
$V$	Voigt
$v_f$	Bulk flow velocity
$V_p$	Probe voltage
$w$	Electron impact parameter
$\alpha$	Atomic polarizability of the neutral perturber, static ion broadening parameter, Debye ratio
$\delta E_U$	Uncertainty in energy
$\delta t$	Finite time difference
$\epsilon_0$	Permittivity of free space
$\lambda$	Wavelength
$\lambda_D$	Debye length
$\mu$	Reduced mass
$\mu_i$	Ion mobility
$\chi$	Probe bias voltage

If I go out into nature, into the unknown, to the fringes of knowledge; everything seems mixed up and contradictory, illogical, and incoherent. This is what research does; it smooths out contradictions and makes things simple, logical, and coherent.

- Albert Szent-Gyorgyi

## CHAPTER 1

### INTRODUCTION

*The good thing about science is that it's true whether or not you believe in it.*

- Neil deGrasse Tyson

Atmospheric microplasma jets (AMPJs) are primarily used in biomedical and material processing applications[1], [2]. Current material processing research efforts are focused on the synthesis of: carbon nanotubes[3]–[9] and other carbon based structures[10], [11]; silicon[12]–[14] and carbon[15] films; metal nanorods[16]–[18]; and metal[19]–[22], carbon[23]–[25], and other types[26]–[28] of nanoparticles. Biomedical research on the other hand is researching: the treatment of cancer cells[29]–[34], the inactivation of bacteria or sterilization[35]–[40], and other general applications[1], [41]–[44].

Microplasmas are plasmas, or ionized discharges, generated on the small scale, typically millimeter or smaller. Microplasmas are governed by Paschen's Law, or  $pD$  scaling, where  $p$  is the pressure and  $D$  is the smallest characteristic dimension of the plasma[24], [45]. Small plasma dimensions allow for the microplasma to be stable at atmospheric-pressure without arcing. Due to their size, microplasmas have different plasma properties than vacuum plasmas. The literature has shown microplasmas have

high electron densities up to  $10^{16} \text{ cm}^{-3}$ [46], nonequilibrium temperatures[47], [48], and non-Maxwellian electron energy distributions[49], [50]. In order to accurately perform plasma diagnostics at atmospheric pressure conditions, these factors must be taken into account.

AMPJs are of a great interest due to their low gas temperature but high electron temperature and charged particle densities, which makes them ideal for a variety of applications. Atmospheric-pressure operation also removes the need for expensive and complicated vacuum equipment required for low pressure plasmas. Therefore, to safely treat living tissue and low temperature materials, it is important to be able to readily determine plasma properties quickly and in-situ.

## **1.1 Problem Statement**

For low-pressure plasmas, physical probes such as Langmuir probes are a common diagnostic tools used to measure plasma properties of electron temperature and electron number density. Physical probes typically have simple data processing and ability for in-situ direct measurements. The measurement of densities and temperatures with Langmuir probes for microplasmas can be difficult due to their small size and high pressure operation. Standard Langmuir probe analysis assumes a collisionless plasma, which is typically not applicable for atmospheric-pressure microplasmas. At high pressure, the plasma becomes collisional as the ion-neutral mean-free-path becomes smaller than the Debye length[51].

Microplasma properties are typically measured using optical diagnostics such as optical emission spectroscopy with collision-radiative models[52]–[54], Stark

broadening[55], or analysis of OH[56] and N<sub>2</sub>[57]–[59] emissions, laser induced fluorescence[60], laser interferometry[61], [62], and Rayleigh scattering[56], [63]. These techniques require databases, mathematical models, and significant post-processing to obtain plasma properties. Commercial programs such as Specair can speed the post-processing with built-in databases and automated spectra fits. Depending on the size and configuration of the plasma, these measurements can also provide both spatial and temporal resolution. An additional challenge in optical AMPJ measurements is the loss of local thermodynamic equilibrium (LTE), which requires careful attention when performing optical measurements[64].

For future industrial or commercial applications, simpler methods with direct measurement or minimal post-processing are desirable for determining plasma properties. Thus Langmuir probes and thermocouples are of interest for their simplicity but their applicability to microplasmas is unknown. Langmuir probes have been used in some microplasma studies, although the results are mixed[55], [65]–[69]. Langmuir probes are a simplistic and cost effective solution to measure electron density and temperature. Optical methods on the other hand can require expensive equipment and detailed models, such as collisional models, in order to accurately measure the electron properties.

Thermocouples are a common tool to measure gas temperatures in many industrial applications. They are inexpensive and provide immediate readings. The difficulty for plasma use though is the presence of charged particles and local electric fields that can interfere with readings. One simple optical method to measure gas temperature is van der Waals or Doppler broadening[45], [64], [70] of neutral emission lines such as ArI. From knowledge of the broadening profile of a spectral line, the gas

temperature can be directly calculated from a single equation. At temperatures  $< 1000$  K, van der Waals has a much larger broadening profile than Doppler. With the large number of ArI lines, there is a need to determine which lines produce accurate and reproducible results and if a relationship exists between the accuracy of individual ArI lines and the experimental configuration.

## **1.2 Research Contributions**

The present research investigates the application of low cost physical probes (Langmuir probes and thermocouples) and optical emissions spectroscopy to atmospheric microplasmas. The goal is to characterize an AMPJ operating with argon gas using physical probes and compare the results to optical techniques. The plasma properties of interest include gas temperature, electron temperature, and electron density. Due to the expected low temperatures of the experimental plasma configuration ( $< 500$  K), van der Waals broadening of argon spectral lines was chosen to measure the gas temperature. Cylindrical Langmuir probes were used to measure the plasma density and electron temperature. This work compares four different methods to determine the accuracy of the temperature measurement: van der Waals broadening of argon spectral lines, spectral fitting of OH (A-X) and N<sub>2</sub> (C-B), and type K thermocouples. Due to equipment limitations, optical measurements of the plasma density and temperature were not possible.

This work aims at providing a highly detailed comparison between the two types of diagnostic techniques; physical probes and optics. Multiple methods for each type are utilized to provide a thorough analysis of the accuracy of current techniques. In addition

to testing different diagnostic methods, two AMPJ configurations are used to determine if the accuracy of results are dependent on the experimental configuration. Finally, the current literature is lacking detailed information regarding the use of multiple ( $> 2$ ) ArI emission lines and the use of identical ArI lines for multiple configurations. Therefore, this study hopes to contribute new information which may be useful to those in the fields of plasma diagnostics and atmospheric-microplasma jets.

## CHAPTER 2

### BACKGROUND

*If I have seen further it is by standing on the shoulders of Giants.*

- Isaac Newton

Plasma diagnostics, or the determination of plasma properties, can be broken down into two general types: optical techniques and physical probes. This research focused on comparing the two types where possible using the following methods: van der Waals broadening of argon spectra lines, spectral fitting of OH (A-X) and N<sub>2</sub> (C-B), type K thermocouples, and Langmuir probes. The following sections of this chapter provide a detailed review of the literature in the methods applied and AMPJs.

#### **2.1 Atmospheric Microplasma Configurations**

There are many different configurations of atmospheric microplasma depending on the power source, geometry, and materials used. The two configurations of interest in this work are dielectric barrier discharge (DBD) and DBD-like plasma jets. A DBD configuration includes a dielectric barrier separating the plasma from the positive and negative electrodes. A DBD-like configuration mimics that of a DBD, just without a dielectric barrier. When the plasma plume is not in contact with an electrically

conducting material, it has almost the same behavior as that of a DBD. But when a non-dielectric material comes too close, the discharge runs from the electrode to the object and the plasma is no longer acting like a DBD. Lu *et al*[71] has provided detailed schematics of both configurations, copies here in Figures 2.1 and 2.2. It is uncommon to find setups utilizing a DBD-like[71] configuration with both central pin and ring electrodes, with some groups opting for an inductively coupled [24], [25], [72] or DBD configurations[70], [71]. The AMPJ used in this work is of the type shown in Figure 2.1a.

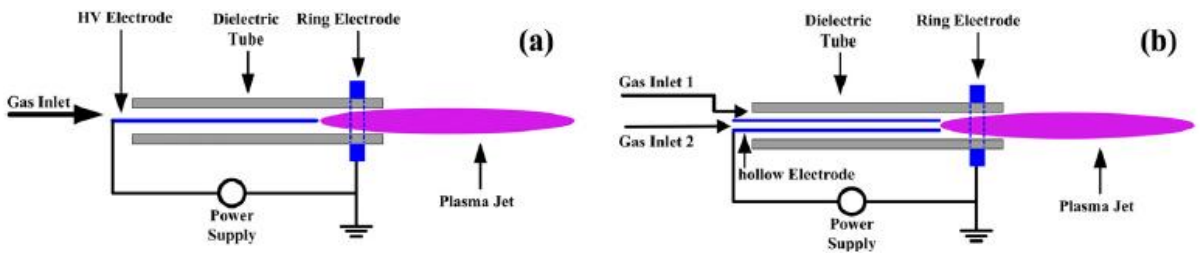


Figure 2.1 Schematics of DBD-like plasma jets [71].

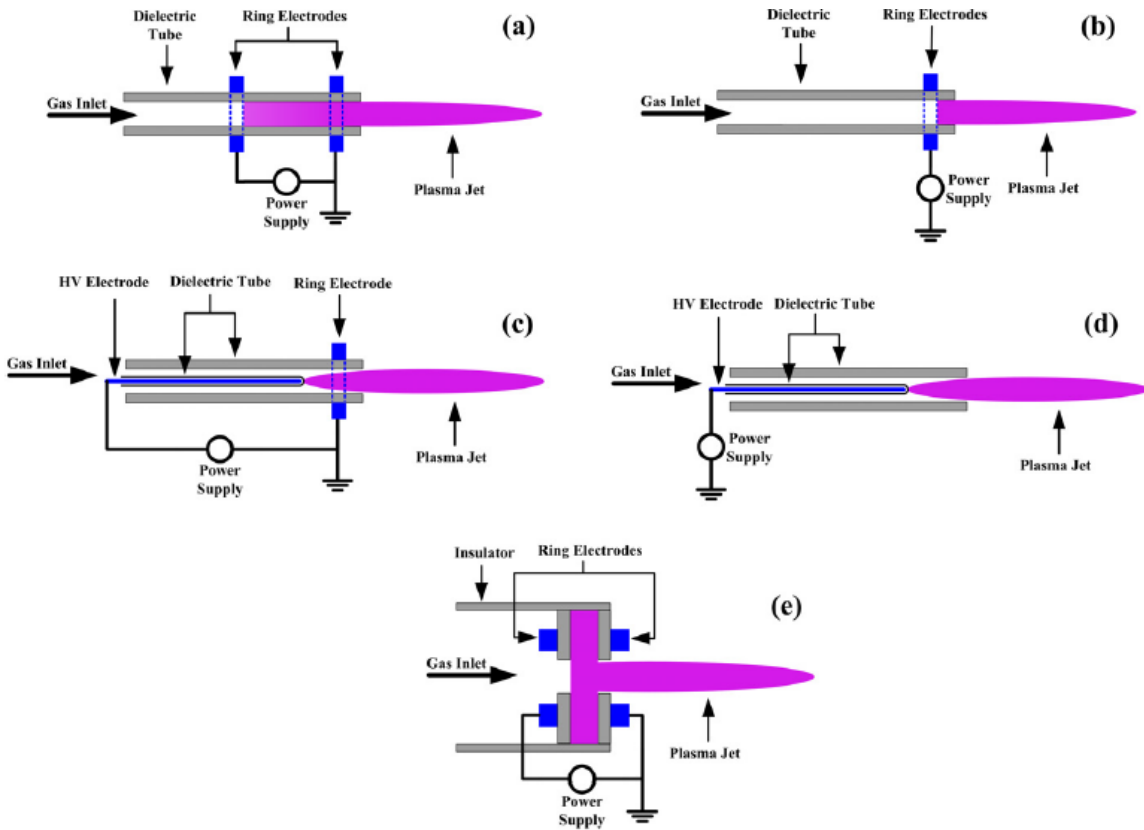


Figure 2.2 Schematics of DBD plasma jets [71].

Experimental setups are typically powered by an RF source operating at high frequency (HF) or ultra-high frequency (UHF)[14], [22], [24], [25], [56], [72]–[74]. With that said, AMPJs can also be driven by ac[71], [74], dc[71], or pulsed dc power[71].

Other types of atmospheric-pressure plasmas exist which are used in the literature primarily for diagnostic studies. These include microwave powered setups[58], [64], [75]–[80], which can be found in a variety of configurations, such as a torch [58], [80], or surface-wave discharge[64], [78], [79].

## **2.2 Review of Literature**

Following is a summary of experimental and numerical results from the literature on the diagnostic methods. The results include determinations of gas temperature, electron temperature, and electron density. Results may vary between authors due to variances in experimental setups and may contradict each other. In addition to reporting the results, differences in experimental setups are noted.

### **2.2.1 Spectral Line Broadening Mechanisms**

Due to non-ideal operating conditions, various broadening mechanisms play a key role in the broadening of emission lines. The dominant broadening mechanisms are: instrument, Doppler, van der Waals, and Stark. There are also resonance and natural broadening, however these contributions are almost always many orders of magnitude smaller that they are often neglected. Instrument broadening is caused by the emissions detection system, which includes the spectrometer, camera, and any intervening optics. Doppler is a consequence of the fact that the emitted line frequency depends on the

velocity of the emitting particle with respect to the detector. Van der Waals comes from the collisions between the emitting species and neutral particles or molecules. Finally, Stark is also a result of collisions, but between the emitting species and charged particles. While instrument broadening is solely dependent on the equipment being used, the other mechanisms are dependent on gas temperature (Doppler, VDW), electron temperature (Stark), and electron density (Stark). Therefore, they can be used to solve for these properties. This process is explained in greater detail with equations in Chapter 3: Experimental Methods.

### **2.2.2 Gas Temperature Determination from van der Waals Broadening**

The literature has showed that the gas temperature can be obtained from argon spectral lines through the use of line broadening techniques[57], [64], [81]–[83]. An advantage of this method is that trace gases do not need to be added to the argon plasma. In this work the measurements were taken in the jet that emanates into ambient air where ambient  $N_2$  and OH are present. For measurements of the plasma in other locations, argon line broadening removes the need for the addition of air, nitrogen, or water vapor. A complete list of argon spectral lines can be found through the NIST *Atomic Spectral Database*[84]. Zhu and Pu[85] compiled a detailed list of useful neutral argon (ArI) transitions from the 2p to the 1s level. Between these and other studies[52], [58], [59], [82], easily identifiable strong intensity spectral lines were chosen. Table 2.1 shows argon wavelength and upper and lower states of spectral lines typically investigated in the literature.

Table 2.1 Common argon spectral lines and their transitions.

Wavelength (nm)	Upper Level	Lower Level	References
750.4	2p <sub>1</sub>	1s <sub>2</sub>	[52], [59], [84]
696.5	2p <sub>2</sub>	1s <sub>5</sub>	[82], [84]
738.4	2p <sub>3</sub>	1s <sub>4</sub>	[52], [84]
706.7	2p <sub>3</sub>	1s <sub>5</sub>	[84]
751.5	2p <sub>5</sub>	1s <sub>4</sub>	[84]
800.6	2p <sub>6</sub>	1s <sub>4</sub>	[84]
763.5	2p <sub>6</sub>	1s <sub>5</sub>	[52], [58], [84]
810.4	2p <sub>7</sub>	1s <sub>4</sub>	[84]
842.5	2p <sub>8</sub>	1s <sub>4</sub>	[84]
801.5	2p <sub>8</sub>	1s <sub>5</sub>	[84]
811.5	2p <sub>9</sub>	1s <sub>5</sub>	[58], [84]

Following the method of Ionascut *et al*[70], the gas temperature can be determined from the van der Waals broadening assuming Stark broadening is negligible or is already known. Stark can be neglected for relatively low electron temperatures and electron densities  $< 10^{16} \text{ cm}^{-3}$ , where collisions between the neutral and emitter species are frequent. The validity of this assumption has been demonstrated by other research groups[45], [64], [70] and is also examined later in this work.

Chen and Li[58] applied van der Waals broadening to the 763.5 nm and 811.5 nm ArI lines for a microwave powered nitrogen-argon torch. For configurations similar to theirs, it was determined that the Stark broadening would be on the order of 0.1 pm[86], [87], in comparison to the calculated van der Waals and Doppler broadening between 5-25 pm[58]. Due to a gas mixture being used, a modified form of the van der Waals broadening FWHM equation was used, shown as

$$\Delta\lambda_{VDW} = 8.18 \times 10^{-26} \times \lambda^2 \times (R^2)^{\frac{2}{5}} \times (T)^{0.3} \times \left[ (\alpha_{Ar})^{\frac{2}{5}} \left( \frac{1}{\mu_{Ar-Ar}} \right)^{\frac{3}{10}} N_{Ar} + (\alpha_{N_2})^{\frac{2}{5}} \left( \frac{1}{\mu_{Ar-N_2}} \right)^{\frac{3}{10}} N_{N_2} \right], \quad (2.1)$$

where  $\lambda$  is the wavelength in nm,  $\alpha$  is the atomic polarizability of the neutral perturber,  $\mu_{Ar-Ar}$  and  $\mu_{Ar-N_2}$  are the reduced masses of the emitter-perturbing pair,  $N$  is the number density of each species in the ground state, and  $R^2$  is the difference of the squared radius of the emitting atom in the upper and lower levels. Van der Waals broadening of the ArI lines was found to result in errors much greater than 10%, in part due to the high temperatures of the plasma (< 5000 K). At high temperatures, the van der Waals broadening FWHM is less sensitive to changes in the gas temperature, yielding inaccurate results. Calculations indicated that the FWHM changes only 0.0005 nm between a temperature change of 5000 K to 6000 K, indicating this method is better suited for low temperature plasmas (< 3000 K). One other problem with this approach is that N<sub>2</sub> molecular bands provide spectral interferences at the expected temperatures, leading to very few ArI lines being resolvable for analysis.

Christova *et al*[64] studied an atmospheric argon surface-wave discharge powered by a microwave source. The van der Waals broadening of the argon species was performed with alternative choices for the ArI lines. Emission lines included the following wavelengths: 737.2, 641.6, 591.2, 560.7, 603.2, 518.8, 549.6, and 522.1 nm. Studies performed by Calzada[78], [79] utilized similar lines also for an argon surface-wave discharge, indicating that these wavelengths may be better suited for those configurations.

The literature has shown that van der Waals broadening can also be applied to hydrogen ( $H_{\alpha}$ [56] and  $H_{\beta}$ [56], [70], [74]) and helium[70], [74] species, although with mixed results. Park *et al*[74] created an atmospheric microplasma jet capable of being operated with ac, pulsed dc, or rf power. The setup utilized argon or helium as the working gas, with trace amounts of oxygen gas fed in. For this study, natural and Stark broadening were also neglected. Two transitions were analyzed to determine the gas temperature of the plasma: 587.5 nm ( $H_{\alpha}$ ) and 486.1 nm ( $H_{\beta}$ ). At 1.75 kV (pulsed dc) and 2 slm of He, van der Waals broadening analysis led to gas temperatures of only 301 K ( $H_{\alpha}$ ) and 306 K ( $H_{\beta}$ ). An increase in temperature up to 330 K was observed when the system was powered by rf. These calculations were found to agree well with measurements obtained from OH rotational line simulation comparisons and the optical fiber thermometer.

Hofmann *et al*[56] studied an rf-driven tungsten needle with both argon and helium gases. A two-electrode system was used with a grounded copper electrode in the center of the tube and a concentric electrode around the outside. The AMPJ was operated in a linear-field configuration[88] at 11.7 MHz.  $H_{\alpha}$  and  $H_{\beta}$  emission lines were recorded and analyzed through van der Waals broadening calculations. Rayleigh scattering was assumed to be the most accurate method to obtain the gas temperature, serving as the baseline for comparison between methods. Results from Rayleigh scattering yielded gas temperatures ranging from 300 K to 600 K, depending on the current. For purely argon plasmas,  $H_{\beta}$  emissions led to severely underestimated temperatures, differing by on average 200 K.  $H_{\alpha}$  calculations led to gas temperatures only 100 K lower than the Rayleigh scattering analysis. For helium-argon plasmas,  $H_{\beta}$  resulted again in

underestimated temperatures roughly 100-150 K lower, while  $H_{\alpha}$  yielded values within the error of the Rayleigh scattering measurements. This behavior is expected due to the fact that the Stark effect is more prominent in hydrogen atoms[89]. When this effect is ignored, as in van der Waals analysis, the calculations can lead to substantially underestimated temperatures. Therefore, Hofmann *et al*[56] concluded that careful consideration must be made when choosing a method to measure the gas temperature.

Finally Ionascut *et al*[70] analyzed He (587.5 nm) and  $H_{\beta}$  (486.1 nm) emission lines for an atmospheric-pressure dielectric barrier discharge (DBD) torch. A pulsed dc power source was used, operating at 10.8 kV. Helium gas was flown through the configuration at 9 slm. These settings were used as they produced the strongest signals with the resolution maximized. The gas temperature was calculated as 460 K for both emission lines, leading to an error of just over 12% based on prior rotational temperature measurements of 533 K[90]. The effect of voltage on the gas temperature was also studied, with voltages ranging from 5.8-10.8 kV. The helium line resulted in temperatures ranging from 315 K to 460 K, with an average temperature increase of 30 K for each additional 1 kV (linear behavior). Hydrogen resulted in similar temperature values at 5.8, 6.8, 9.8, and 10.8 kV, while showing only a minor deviation at 7.8 kV and 8.8 kV. Overall, the two lines yielded similar results. Both lines yield accurate temperature values, in relation to the prior rotational temperature measurements[90], at voltages ranging from 5.8-7.8 kV. Higher voltage readings resulted in an underestimate, although with error values peaking at 12%.

Very little literature was observed which detailed the use and comparison of more than two ArI lines. In addition, no literature was found detailing the impact of AMPJ configuration on the accuracy of ArI lines.

### **2.2.3 Gas Temperature Determination from OH and N<sub>2</sub>**

One of the most commonly used methods to determine the temperature of a plasma or high temperature gas is via the rotational spectrum of diatomic molecules. The traditional concept of gas temperature arises from the translational motion or energy of particles. A particle has up to four energy modes: translation, rotation, vibration, and electronic. Atoms only have translation and electronic energies while diatomic and large molecules have all four modes. From kinetic theory, the rotational and translational energy modes are almost always in equilibrium owing to only a few collisions necessary to transfer energy between the modes. Thus the rotational temperature can often be assumed equal to the translational temperature. The rotational modes of diatomic molecules have well characterized emission spectra, thus can be measured.

A positive benefit of AMPJs is that the discharges operate in open air, allowing for impurities such as water and nitrogen to be naturally present in the jet. The OH (A-X) emission band is frequently used to determine the gas temperature due to its strong emission and easy detection[1], [56], [91]–[94]. While less common, the N<sub>2</sub> (C-B) emission band can also be used[58], [92], [93], [95]. Simulations can be used to generate theoretical rotational spectra for different rotational temperatures, allowing for simple comparisons. Specair[56], [58], [93], [94] and Lifbase[56], [58] are the most commonly used simulation programs in the literature.

The R<sub>1</sub> and Q<sub>1</sub> branches of OH between 306-312 nm and the N<sub>2</sub> rotational lines with a  $\Delta v = -3, -2,$  and  $-1$  between 334-405 nm are commonly used for temperature measurements. Simulated spectra can be obtained from commercial programs such Specair[94] and Lifbase[96]. Figures 2.3 and 2.4 show simulated spectra generated by Specair at a gas temperature of 400 K for OH (A-X) and N<sub>2</sub> (C-B), respectively. While Specair has databases for both OH and the N<sub>2</sub> second positive system, Lifbase can only calculate the OH spectra, but is available as freeware. Lifbase can simulate the first negative system of N<sub>2</sub><sup>+</sup>, but those peaks were not observable in this work due to the low energies and use of ambient nitrogen.

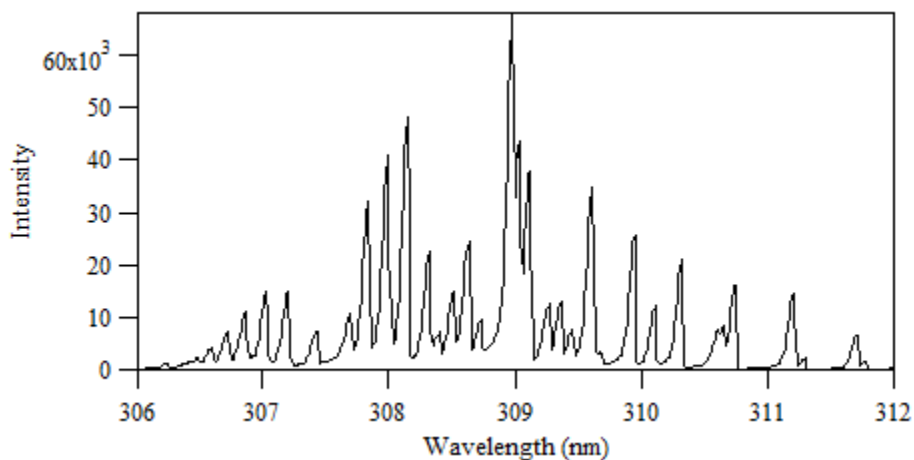


Figure 2.3 OH (A-X) simulated spectrum using Specair.

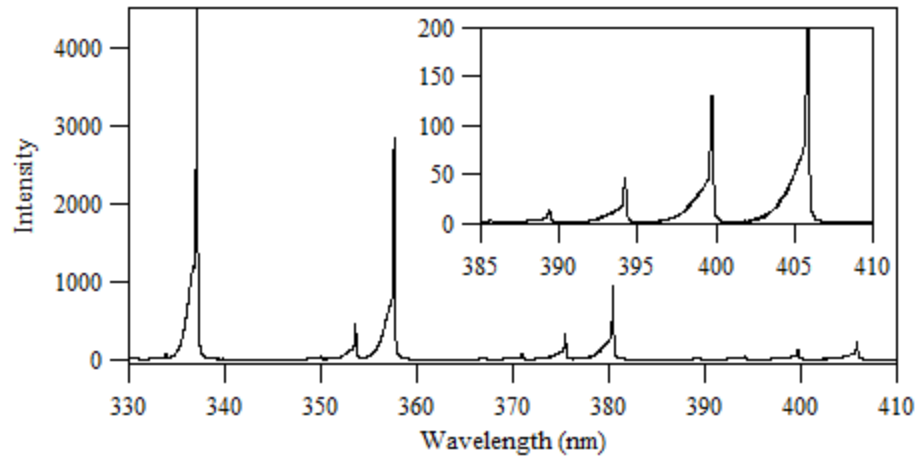


Figure 2.4 N<sub>2</sub> (C-B) simulated spectrum using Specair. The inset figure shows a magnified view of the spectrum from 385-405 nm, representing the  $\Delta\nu = -3$  lines.

A common assumption of these simulated spectra is that the rotational lines have a Boltzmann population distribution[94], [96]. Boltzmann plots can be generated to determine if there is a Boltzmann population distribution. If the plot yields a linear line, the rotational states follow a Boltzmann population distribution. This is a valid assumption for most atmospheric pressure plasmas[56] and has also been assumed for this work.

Aside from using van der Waals broadening, Hofmann *et al*[56] also compared the effectiveness of Boltzmann plots of OH (A-X) for accurate gas temperature measurements. Results were mixed depending on the chemical composition of the plasma. For an argon plasma, OH (A-X) plots yielded temperatures slightly larger than the Rayleigh scattering results, but within the error. For a helium-argon plasma, the OH (A-X) temperatures were greatly overestimated, being an average of 250 K higher than expected. Finally, results for a helium plasma also yielded greatly elevated temperatures. One reason the authors gave for the overestimation of the gas temperature is that the

configuration may have a high electron temperature. For helium plasmas, this results in the increase of the non-equilibrium of the OH (A-X) distribution[97].

Chen and Li[58] studied three nitrogen transitions: N<sub>2</sub> (C-B), the second positive band; N<sub>2</sub> (B-A), the first positive band; and N<sub>2</sub><sup>+</sup> (B-X), the first negative band. The second positive system, while often used, is highly problematic and inaccurate. Spectral overlap exists with the first negative system and the NH (A-X) band, leading to potential issues[58]. The N<sub>2</sub> (C) population can also easily be modified in the presence of argon, leading to the deviation of the rotational populations from a Boltzmann distribution[95]. Finally, the emissions profile is highly sensitive to low electric fields, leading to incorrect temperature readings[93], [98]. The last two points will be discussed in greater detail later in this study. The first positive system is characterized by high emission intensities and minimal perturbations by neighboring states[58], [99]. For high rotational temperature systems though, the first positive system is too insensitive to be used accurately[58]. The first negative band is favored when used for determining the rotational temperature by spectra synthesis fitting. With that said, small mismatches of the positions of spectral lines and line widths can lead to large residual values when fitting experimental spectrum with simulated ones[64]. This can lead to uncertainty values of over 10%[100]–[102]. The first negative band requires there is no spectral overlap and a minimum spectrometer resolution[58].

Commercial simulation programs such as Specair and Lifbase assume an equilibrium Boltzmann distribution of the rotational states in order to accurately determine the rotational temperature. According to Hofmann *et al*[56], this is a valid assumption for most atmospheric pressure plasmas since the excited states have a large

number of collisions. Bruggeman *et al*[91], [92], [103] however has shown though that some atmospheric pressure plasmas have rotational states which do not follow an equilibrium Boltzmann rotational population distribution. This is primarily a result of complex population mechanisms which reduce the lifetime of the excited states. Work by Verreycken *et al*[92] has also shown that an overestimate of the gas temperature can be made even when the rotational states follow the Boltzmann distribution.

Two studies conducted by Bruggeman *et al*[91], [103] which showed this deviation from ideal behavior, focused on the incorporation of liquids into atmospheric plasmas. In the first study[91], a rf He-water glow discharge was generated. Electronic quenching of OH (A-X) was observed, which prevented the equilibration of the rotational population distribution. Due to this behavior, a two temperature fit was utilized which took into account the parameters  $T_1$ ,  $T_2$ , and the percentage of distribution with temperature  $T_1$  or  $T_2$ . The values of  $T_1$  and  $T_2$  were solved by comparisons between experimental data and Lifbase simulations, yielding values of 350 K and 15000 K, respectively. The baseline gas temperature was measured at 350 K, leading to the conclusion that the observed emission band is only a partial representation of the true gas temperature. In the second study[103], liquid electrodes were tested for a glow discharge. The rotational population distribution was found to be influenced by the processes, leading to an inaccurate representation of the kinetic temperature. Verreycken *et al*[92] confirmed these inaccuracies when a water electrode was used for a glow discharge. Measurements of gas temperature from OH (A-X) emissions were found to deviate from Rayleigh scattering calculations by over 1000 K. With that said, it was determined that  $N_2$  (C-B) emissions provided a more reliable measurement of the gas temperature. Based

on the results of these studies, the use of liquids in atmospheric-pressure plasmas may lead to incorrect gas temperature values when using the OH (A-X) spectra.

A high temperature ( $T > 2000$  K) glow discharge generated by a dc electric field was studied by Laux *et al*[94]. Spectra of interest included OH (A-X) and N<sub>2</sub> (C-B). Due to the possibility of quenching of the rotational levels of OH (A-X), a verification method was needed to verify that the rotational levels followed a Boltzmann distribution. Instead of generating a Boltzmann plot, as typically done in the literature, the experimental data was compared to spectra simulations. Based on the fact that a simulation was found to match the emission spectra, it was determined that the rotational levels followed a Boltzmann distribution. Analysis of the N<sub>2</sub> (C-B) spectra with simulations yielded results consistent with that of the OH (A-X); 2200 K and 2250 K, respectively.

#### **2.2.4 Electron Properties from Stark Broadening of Hydrogen**

Direct methods to measure these properties are preferred as no assumptions need to be made about particle distributions or ionization and excitation states. A common direct method, called Thompson scattering, can be difficult and expensive to implement[75]. Work by Torres *et al*[75], [104], [105] investigated the simultaneous measurement of electron temperature and electron density through analysis of two or three hydrogen emission lines. This method is also known as the hydrogen cross point method. In comparison to Thompson scattering, which is accurate and precise with both spatial and temporal resolution, the Stark broadening of hydrogen can be less accurate with a somewhat high uncertainty. One disadvantage is that it has a lower limit of measurable density.

Torres *et al*[75] studied a microwave powered surface wave discharge. The Stark broadening of  $H_{\beta}$  and  $H_{\gamma}$  were determined through a de-convolution of the measured Voigt emissions profile. The calculated Stark values were then used to plot the electron temperature versus the electron density for each hydrogen line, through the use of the Generalized Kohn-Sham (GKS) theory[106], [107]. Based on the crossing point of the two lines, the electron temperature and density were determined to be between 3400-4600 K and  $5.7-9.2 \times 10^{14} \text{ cm}^{-3}$ , respectively, given varying microwave power levels.

In order to test the accuracy of the GKS theory, an additional theory, the Gig-Card theory[108], [109], was used as a comparison. While GKS theory ignores ion dynamics, the Gig-Card theory includes ion dynamics as an additional source of collisional broadening. The electron temperature and density, using the Gig-Card theory, were determined to be between 5100-8000 K and  $5.3-8.1 \times 10^{14} \text{ cm}^{-3}$ , respectively, given varying microwave power levels. While the electron densities were relatively close, there was a noticeable difference in the electron temperature calculations from the GKS results. Error values were estimated to be 40% of the order of magnitude due to limitations of the individual theories and experimental error. Results obtained with the Gig-Card theory were in better agreement with other experimental results previously obtained for similar configurations[110]–[112]. This was expected as the theory is further developed and is more mathematically intensive. It appears though that the GKS theory can be applied to obtain an accurate estimate of the electron density.

Other studies by Torres *et al*[104], [105] have utilized three hydrogen emission lines:  $H_{\beta}$ ,  $H_{\gamma}$ , and  $H_{\alpha}$ . Due to better accuracy in measurements with the Gig-Card theory, the GKS theory was not used. In either study, no point is found which corresponds to all

three hydrogen lines crossing at once. With that said, a general crossing region can be determined by boxing around all of the individual points of crossing. The individual locations were found to correspond to similar electron densities, but varying electron temperatures. The experimental error was determined to be only 5% for the electron density, but as high as 40% for the electron temperature.

While the  $H_\alpha$  and  $H_\delta$  lines can be used for the cross point method, they are typically avoided unless necessary. As noted by Torres *et al*[75], low quantities of hydrogen can yield minimal  $H_\delta$  line intensities. The addition of large quantities of hydrogen though can disturb the plasma discharge greatly, yielding poor resolution of the line. While  $H_\alpha$  is the most intense line of the Balmer series, some problems do exist. These include self-absorption and a lack of an appropriate theoretic description of its Stark broadening. Work by Griem[113] and Gigosos[109] has shown the theoretical predictions of the line-shape do not agree with experimental results, in part due to polarization changes stemming from complex internal structures[75], [114].

### **2.2.5 Langmuir Probes**

Physical probes, such as Langmuir probes, have been used for high pressure systems in some studies[115]–[120] but with mixed results. Careful consideration must be made when using Langmuir probes with rf systems as additional noise can be generated, although this can be filtered out by modifying the setup. Prior studies on this configuration have been completed by Xu and Doyle[51], with single and double Langmuir probes used to measure the electron density and temperature, respectively. A 6 mm OD and 2 mm ID quartz tube was used with argon gas flowing at 0.5-2.0 slm. The rf

power, operating at 13.56 MHz, was varied from 30-70 W. Electron temperatures and densities were measured at distances of 2.5-6.5 mm in increments of 1 mm. The electron temperature was found to increase with both distance and flow rate. The highest temperatures were observed at 30 W, indicating that lower powers produce higher electron temperatures. It has been suggested that this behavior is due to faster recombination of low energy electrons and increased flow mixing at high velocities. At 2 slm, the electron temperatures were calculated to be 3.0-4.4 eV. While 30 W produced the highest temperatures, it was observed that 70 W yielded higher values than 50 W. An uncertainty of  $\pm 15\%$  was used due to uncertainty in the average data sets and the radial probe location.

The regime criteria were solved to determine the regimes the plasmas were operating in. Due to varying flow rates, it was determined that the plasma starts in the stationary regime at 0.5 slm, but transitions to the flowing regime at 1 and 2 slm. All probes tested at 1 and 2 slm were determined to be in the thick sheath-convection regime. Probes for the 0.5 slm tests operated in the thick stationary regime. At 2 slm, the density was measured between  $10^{16}$ - $10^{19}$   $\text{m}^{-3}$ . The density was found to decrease with distance, with the maximum occurring at 50 W. At 30 and 50 W, the highest plasma density was observed at 1 slm. A constant density was observed across all flow rates at 70 W. An uncertainty of  $\pm 30\%$  was used based on the work of Clements, whose solution has an inherent 30% uncertainty.

## CHAPTER 3

### EXPERIMENTAL METHODS

*Your assumptions are the windows on the world. Scrub them off every once in a while, or the light won't come in.*

- Isaac Amisov

#### 3.1 Experimental Setup

The experimental setup is composed of the following systems: rf power supply, sourcemeter, thermocouple reader, and optical emission spectrometer. A general diagram of the overall setup is shown in Fig. 3.1. Each is discussed in further detail in the following sections.

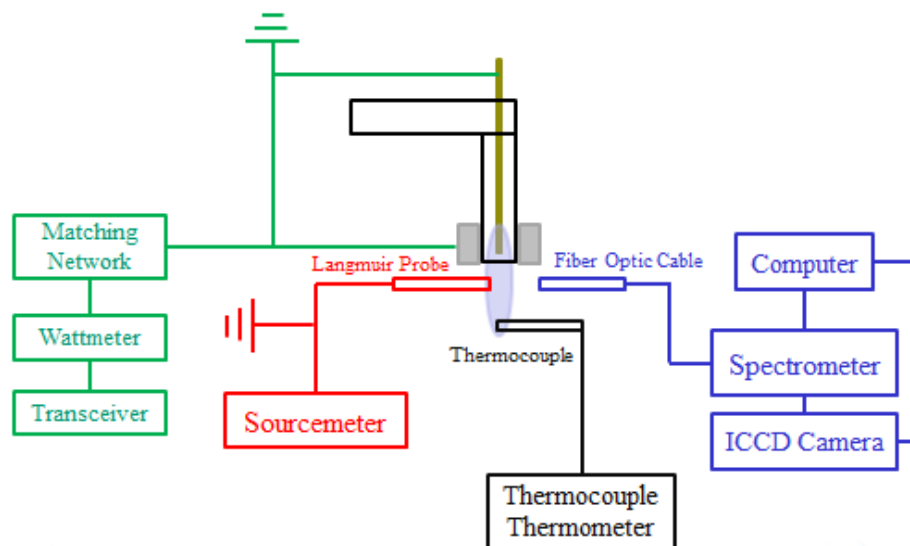


Figure 3.1 Diagram of complete experimental setup.

A schematic of the AMPJ experiment is shown in Fig. 3.2 and 3.3. The plasma was generated in a 6 mm outer diameter (OD) and 3 mm inner diameter (ID) quartz tube with a 1 mm diameter central tungsten pin electrode. An external stainless steel collar with a 7 mm ID and 8 mm length placed near the exit of the quartz served as the second electrode. Argon gas was flowed through the quartz tube at a constant rate of 2 liters per minute with a MKS mass flow controller. The plasma was operated at 14 MHz using a FT 950 radio transceiver, an AT5K matching network, and an LP-100A wattmeter. The plasma was tested at forward rf powers of 50, 70, and 90 W. The transceiver has a maximum power of 100 W. For all measurements, the power was maintained at  $\pm 0.5$  W and the standing wave ratio (SWR) was kept  $\leq 1.05$ . All temperature measurements were taken of the microplasma jet that emanated directly into open air.

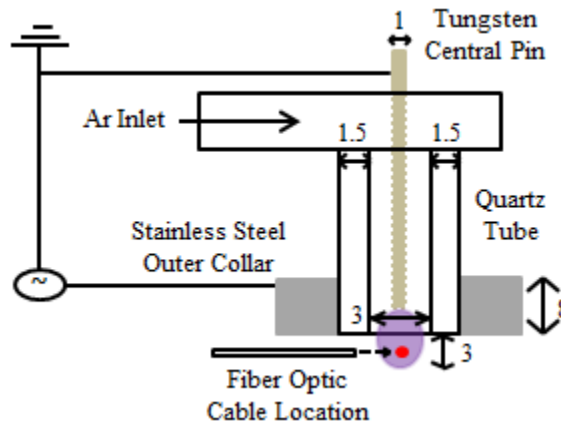


Figure 3.2 Schematic of the experimental setup. All dimensions are in mm. The red dot represents the location of the thermocouples.

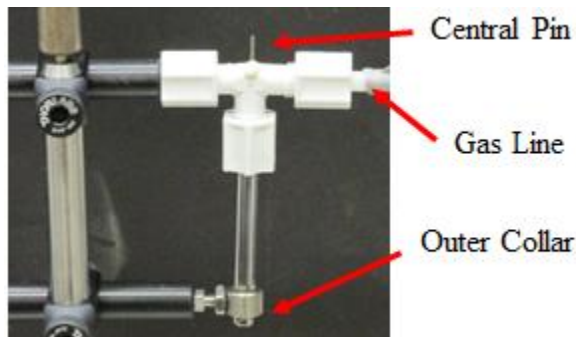


Figure 3.3 Picture of actual experiment.

The argon lines of interest were selected based on a detailed review of the current literature as well as preliminary analysis of OES data collected. The lines chosen included 696, 706, 738, 751, 800, 810, 811, and 842 nm, which all originate from 2p-1s transitions. Two different type-K thermocouples (T/C) were used. The first was a bare bead attached to the bottom of a 2 mm thick Pyrex plate with adhesive, and the second was a 1/16" Inconel sheath and ungrounded T/C. They are referred to as the "adhesive" and "shielded" in the results. The T/C's were placed 3 mm below the tube exit centered directly under the jet. They were given 10 minutes to reach a stable temperature before measurements were read after disabling the rf power source, which can cause interference. Fig. 3.4 shows an example of a bare bead thermocouple.

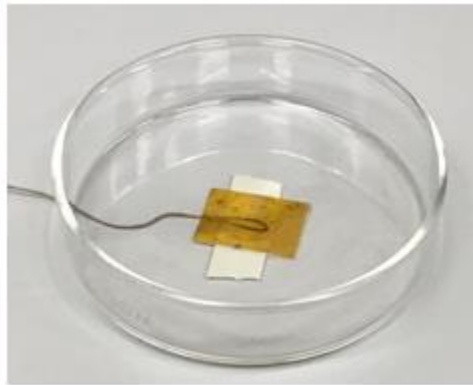


Figure 3.4 Sample image of an adhesive bare bead thermocouple.

The emission spectra were captured with a fiber optic cable connected to an Acton SP2500 spectrometer with a 500 mm focal length, 1200 g/mm grating, and a PI-MAX4 ICCD camera. The entrance slit width was set to 70  $\mu\text{m}$  and the resolution was 0.0409 nm/pixel. The spectrometer and fiber were calibrated for both wavelength and intensity using Princeton Instrument's IntelliCal spectral calibration system. 300 images were taken for each spectra and averaged to produce a final raw spectrum. A total of 9

averaged raw spectra were obtained for each measurement. The programs Specair and Lifbase were used to simulate the spectra of OH and N<sub>2</sub>, and Igor Pro was used to obtain fits of the argon lines. The optical fiber was fixed at 3 mm from the exit of the quartz tube for all emission spectra measurements.

### 3.1.1 AMPJ Electrode Configurations

Two AMPJ configurations were tested. The first configuration had the center tungsten pin grounded and the stainless steel collar connected to the rf signal, which is referred to as a linear-field jet[88]. The second configuration had the center tungsten pin connected to the rf signal and the outer collar grounded, which is referred to as a cross-field jet[88]. The wiring diagrams for each setup are shown in Fig. 3.5 and 3.6. All temperature determination methods were used for both configurations. However, only the adhesive T/C was used on the cross-field configuration due to arcing issues when using the Inconel shielded T/C.

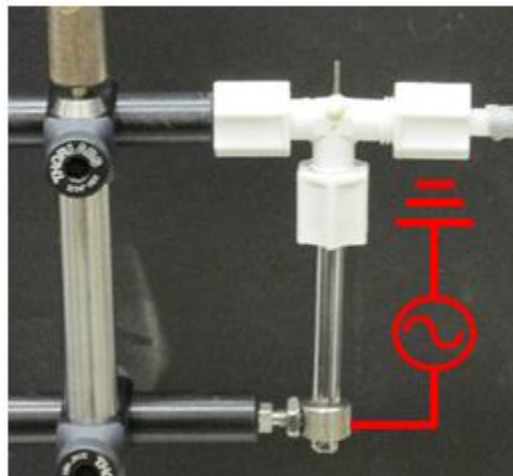


Figure 3.5 Linear-field wiring diagram.

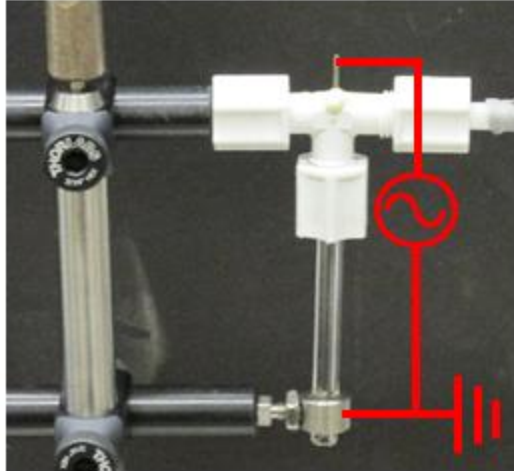


Figure 3.6 Cross-field wiring diagram.

### 3.1.2 Spectra Analysis Software

Specair and Lifbase were used for spectra analysis to simulate OH (A-X) and N<sub>2</sub> (C-B) emission profiles and compare to experimental data. Specair utilized an automated solver, while Lifbase required the simulation comparison to be done by the user. Specair and Lifbase were only used to study the gas temperature of the plasma jet. Igor Pro was used not only to make the graphs shown in this study, but also to analyze the emission peaks and determine the Voigt fit results (FWHM). Finally, MATLAB was used as the iterative solver required to find the gas temperature. The built in MATLAB function *fzero* was used as the solver.

### 3.1.3 Langmuir Probes

The plasma density and electron temperature along the centerline of the emanating plasma jet was measured using single and double Langmuir probes following the method used by Xu and Doyle[51]. The probes were placed 2-6 mm from the exit of

quartz tube, as shown in Fig. 3.7. Single Langmuir probes were constructed from 2 mm long, 0.127 mm diameter tungsten filaments protruding from a 1.6 diameter alumina tube. Double Langmuir probes were constructed of identical tungsten filaments, but with a 2.4 mm diameter alumina tube and a filament separation of 1.3 mm. Layers of Kapton and Glass Cloth electrical tape were added to the bottom of the probes to hold wires in place. Finally, a small amount of ceramic paste (Aremco Ceramabond 571) was applied to the tip of the probe to hold the filament in place. Fig. 3.8 shows an example of a single Langmuir probe.

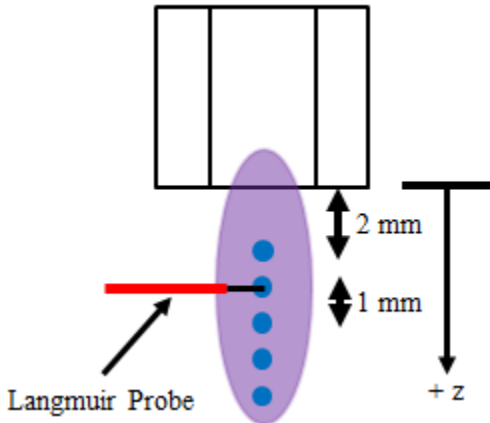


Figure 3.7 Probe locations in the plasma.



Figure 3.8 Example of a single Langmuir probe used in this study.

Probes were mounted on a Velmex linear motion stage and inserted into the plasma. The probe voltage was varied with a Keithley 2400 sourcemeter and the resulting filament current was measured. A custom RF choke was placed in line between the probe and sourcemeter to remove any RF noise pickup. The choke consisted of a grounded metal box with grounded BNC feedthroughs. The signal wire from the probe was carried in a coaxial cable to and from the choke. The coaxial cable shield was grounded to the box while the central pin was wrapped 25 times around a toroidal ferrite (M type). This produces high impedance and filters the rf noise in the lines. Three measurements were taken and an average current was determined at each voltage step, with a delay of 0.3 s between each voltage step. In order to further reduce error, three voltage sweeps were taken at each operating condition and averaged. The final set of data was smoothed before analysis using a locally weighted scatter plot smoothing method.

## **3.2 Diagnostic Theory**

### **3.2.1 Optical Emission Spectroscopy Spectral Line Shape**

Optical emission spectroscopy can be applied to calculate electron density, electron temperature, and gas temperature. This is accomplished by analyzing the broadening of the emission spectra for the species of interest. According to Ionascut *et al*[70], both dependent and independent sources of broadening exist. Independent sources include natural and instrumental broadening, which do not depend on the on the plasma plume properties. Dependent sources, which are affected by the properties of the plasma plume, include resonance, Doppler, Stark, and van der Waals. Sources can also be classified by their line shape as either Gaussian or Lorentzian. Gaussian fits assume that

the distribution has no outliers, while a Lorentzian fit has more pronounced tails. A Voigt profile is a convolution of both Gaussian and Lorentzian fits. Each of these profiles are visually shown in Fig. 3.9. Finally, all broadening components are discussed in terms of the full width at half maximum (FWHM), or the width of the peak at a height of half of the maximum intensity value.

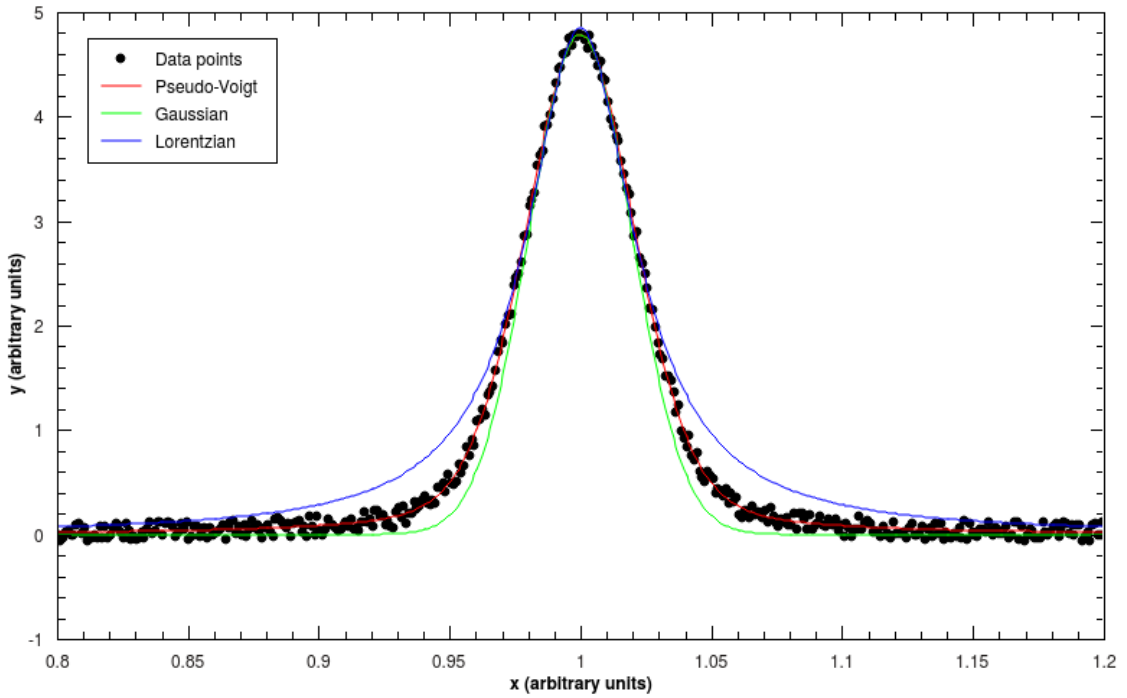


Figure 3.9 Examples of each of the relevant fit profiles.

### 3.2.1.1 Natural Broadening

Natural broadening is a result of the finite lifetime of an unperturbed level,  $\tau$ , due to spontaneous emission. The wavelength of an emitted photon can be expressed in terms of the upper and lower levels, shown as

$$h\nu = \frac{hc}{\lambda} = E_U - E_L, \quad (3.1)$$

where  $h$  is Planck's constant,  $c$  is the speed of light,  $\lambda$  is the wavelength, and  $E$  is the energy with respect to the upper,  $U$ , and lower,  $L$ , levels. The upper energy level is measurable only for a finite time when it exists in that state. There is an inherent uncertainty in the measurement of that energy, which can be expressed using the Heisenberg Uncertainty Principle as

$$(\delta t)(\delta E_U) \sim h, \quad (3.2)$$

where  $(\delta t)$  is the finite time related to the uncertainty in the energy of the upper level,  $(\delta E_U)$ . The time that an atom stays in the upper level though is not fixed as different atoms will have different transition times. Therefore, an average time an atom spends in the upper level,  $\tau_r$ , is used. The spectral line is represented by a Lorentz curve, with a FWHM equal to [86]

$$\lambda_{natural} = \frac{\lambda^2(\sum_m A_{m'm} + \sum_n A_{n'n})}{2\pi c}, \quad (3.3)$$

where  $\lambda_{natural}$  is the FWHM, and  $A_{m'm}$  is the transition probability between the state  $m$  and any other intermediate level  $m'$ . According to Konjević[86], natural broadening is the largest when one of the two levels is dipole-coupled to the ground state, although only resulting in values on the order of  $10^{-4}$  nm. Natural broadening is typically a concern for low electron density plasmas generated in a low-pressure discharge[86]. For atmospheric-pressure conditions, natural broadening is too small to be detected and normally is not taken into account[70].

### 3.2.1.2 Resonance Broadening

Resonance broadening is due to collisions between similar particles where the perturber's initial state is connected by an allowed transition to the upper or lower state of

the radiative transition under consideration[94]. Three transitions are considered for this calculation:  $g \rightarrow l$  (ground to lower),  $g \rightarrow u$  (ground to upper), and  $l \rightarrow u$  (lower to upper). Griem[121] has expressed the FWHM as

$$\Delta\lambda_{res} = \frac{3e^2}{8\pi^2\epsilon_0 m_e c^2} \lambda_{ul}^2 \left[ \lambda_{lg} f_{gl} \sqrt{\frac{g_g}{g_l}} n_g + \lambda_{ug} f_{gu} \sqrt{\frac{g_g}{g_u}} n_g + \lambda_{ul} f_{lu} \sqrt{\frac{g_l}{g_u}} n_l \right]. \quad (3.4)$$

More information about the variables of this equation can be found in the work of Griem[121] and Laux *et al*[94]. For argon plasmas, the literature typically assumes that the resonance broadening is negligible[70].

### 3.2.1.3 Instrument Broadening

The broadening caused by the instrument includes the spectrometer, camera, and any intervening optics. Theoretical calculation of instrument broadening is very difficult and not typically done. Instead, the instrument broadening is easily determined by measuring the broadening of a monochromatic laser. Studies from the literature using argon typically choose a HeNe laser, which operates at 632.8 nm, due to its ease of operation, low cost, and close proximity to key argon emission lines. The instrument contribution can be calculated by observing the laser and determining the FWHM of the Gaussian fit of the emissions. The Gaussian fit of the He-Ne line is shown in Fig. 3.10.

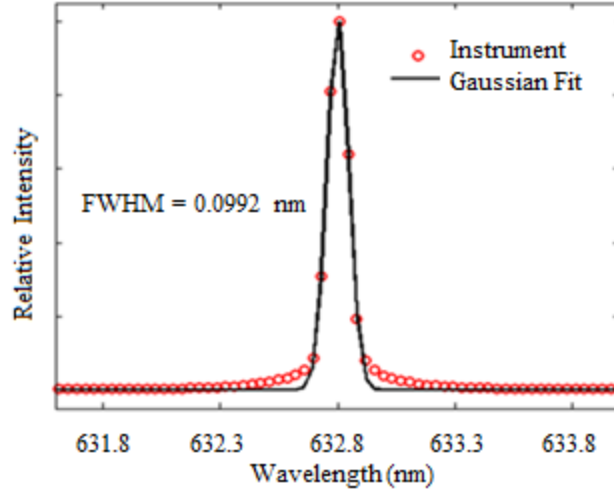


Figure 3.10 Example He-Ne laser emissions spectra centered at 632.8 nm from this work. The plot shows both the spectral data and the resulting Gaussian fit with the corresponding FWHM.

#### 3.2.1.4 Doppler Broadening

Doppler broadening is a consequence of the fact that the emitted line frequency depends on the velocity of the emitting particle with respect to the detector[70]. The Doppler broadening is expressed as[70]

$$\Delta\lambda_{Doppler} = 7.16 \times \lambda \times \sqrt{\frac{T}{M}}, \quad (3.4)$$

where  $\Delta\lambda_{Doppler}$  is the FWHM and  $\lambda$  is the emission wavelength, both in angstroms,  $T$  is the gas temperature in K, and  $M$  is the atomic mass in g/mol. As with instrument broadening, Doppler broadening is represented by a Gaussian distribution.

#### 3.2.1.5 van der Waals Broadening

Van der Waals broadening is a form of pressure broadening, which comes from collisions between the emitting species and neutral particles or molecules. This form of broadening has a Lorentzian distribution and is given by[70]

$$\Delta\lambda_{VDW} = 4.09 \times 10^{-13} \times \lambda^2 \times (\alpha R^2)^{\frac{2}{5}} \times \left(\frac{T}{\mu}\right)^{0.3} \times n, \quad (3.5)$$

where  $\Delta\lambda_{VDW}$  is the FWHM in angstroms,  $\alpha$  is the average polarizability of the neutral perturbers in  $\text{cm}^3$ ,  $R^2$  is the mean square radius of the emitting atom in  $\text{cm}^2$ ,  $\mu$  is the reduced mass of the emitter-perturber system in g/mol, and  $n$  is the perturber density in  $\text{cm}^{-3}$ . The mean square radius is expressed by[70]

$$R^2 = R_{upper}^2 - R_{lower}^2. \quad (3.6)$$

The lower and upper states can be further expressed by using the Unsold hydrogenic approximation[122], which is[70]

$$R^2 = \frac{1}{2} n^{*2} [5n^{*2} + 1 - 3l(l+1)] a_0^2, \quad (3.7)$$

where  $l$  is the orbital quantum number,  $a_0$  is the Bohr radius, and  $n^*$  is the effective quantum number expressed as[70]

$$n^{*2} = \frac{E_{ion}^H}{E_{ion}^{emitter} - E}. \quad (3.8)$$

In Eq. 3.8,  $E_{ion}^H$  is the hydrogen ionization energy,  $E_{ion}^{emitter}$  is the emitter ionization energy, and  $E$  is the excitation energy level involved in the transition. The hydrogenic approximation is special in that it retains the term  $1 - 3l(l+1)$ . The non-hydrogenic approximation therefore does not require knowledge of the orbital angular momentum quantum number.

### 3.2.1.6 Stark Broadening

Stark broadening is the second form of pressure broadening, which comes from collisions between the emitting species and charged particles. For non-hydrogen atoms, the FWHM of the Stark broadening in angstroms is[70]

$$\Delta\lambda_{Stark} = 2 \times 10^{-16} w N_e \left[ 1 + 1.75 \times 10^{-4} N_e^{\frac{1}{4}} \alpha \left( 1 - 0.068 N_e^{\frac{1}{6}} T_e^{\frac{1}{2}} \right) \right], \quad (3.9)$$

where  $w$  is the electron impact parameter,  $N_e$  is the electron density in  $\text{cm}^{-3}$ ,  $\alpha$  is the static ion broadening parameter, and  $T_e$  is the electron temperature in K. The electron impact and static ion broadening parameters are tabulated for various temperatures by Griem[123]. If the ionic contribution is neglected, then the Stark broadening equation can be written as[70]

$$\Delta\lambda_{Stark} = 2 \times 10^{-16} w N_e. \quad (3.10)$$

For hydrogen, the Stark broadening equation is simplified through using the  $H_\beta$  transition and is expressed as[70]

$$\Delta\lambda_{Stark} = 2.5 \times 10^{-9} \alpha_{m,n} N_e^{\frac{2}{3}}, \quad (3.11)$$

where  $\alpha_{m,n}$  is calculated for different  $T_e$  and  $N_e$ [124]. Stark broadening also has a Lorentzian distribution.

### 3.2.1.7 Voigt Profile

The Gaussian and Lorentzian broadening components can be combined through a convolution, which results in a Voigt profile expressed by[70]

$$\Delta\lambda_G^2 = \Delta\lambda_V^2 - (\Delta\lambda_V \times \Delta\lambda_L). \quad (3.12)$$

Thus by separating out the instrument and Doppler from the measured Voigt profile, and assuming negligible Stark, the gas temperature can be calculated from Eq. 3.12 and the remaining van der Waals component. After measuring the Voigt profiles of each argon line and taking into account the instrument contribution, Eq. 3.12 becomes a function of only the gas temperature. An iterative solver can be used to determine the value.

### 3.2.2 Boltzmann Plot

The relative intensities of isolated lines of a rotational spectra can be expressed by

$$I_{rel} \propto \frac{A_{JJ'}(2J+1)}{\lambda_{JJ'}} \exp\left(-\frac{E_J}{kT_{rot}}\right), \quad (3.13)$$

with  $J$  and  $J'$  as the rotational quantum numbers of the upper and lower states, respectively,  $A_{JJ'}$  as the Einstein coefficient[125],  $E_J$  as the energy of the upper level[126],  $k$  as the Boltzmann constant, and  $T_{rot}$  as the rotational temperature. If the slope of the plot of  $\ln[I_{rel}\lambda_{JJ'}/A_{JJ'}(2J+1)]$  as a function of  $E_J$  is linear, then the rotational states have a Boltzmann distribution. The slope can also yield the rotational temperature of the spectrum, although Verreycken *et al*[92] has shown that the Boltzmann plot method may lead to an overestimation of the gas temperature even if the rotational states show a Boltzmann distribution. Einstein coefficients and upper level energies have been reported by Laux and Kruger[127] and Gilmore *et al*[128], respectively.

### 3.2.3 Hydrogen Cross Point Method

The cross point method allows for the simultaneous determination of both the electron temperature and electron density from the analysis of two hydrogen emission lines. Following the methods of Torres *et al*[75], the  $H_\beta$  and  $H_\gamma$  lines are used, centered at 486.1 nm and 434.1 nm, respectively. Other lines such as  $H_\alpha$  or  $H_\delta$ , centered at 656.3 nm and 410.2 nm, can also be used. By using GKS theory[106], [107], the Stark broadening can be used to estimate both electron properties through

$$n_e = \left[ \frac{\Delta\lambda^{Stark} \times 10^9}{2.5\alpha_{\frac{1}{2}}} \right]^{\frac{3}{2}}, \quad (3.13)$$

where  $n_e$  is expressed in  $\text{cm}^{-3}$ ,  $\Delta\lambda^{Stark}$  is measured in nm, and  $a_{1/2}$  is the fractional semi-half-width. The fractional semi-half-width is tabulated for different values of electron temperatures and densities[123], meaning that interpolation can be used to determine missing values. One important caveat is that GKS theory ignores ion dynamics, which can alter the accuracy of the calculations.

$H_\beta$  and  $H_\gamma$  lines are used due to their behavior as a function of both electron density and temperature. At a given electron density, the Stark broadening decreases with electron temperature for  $H_\beta$ , while it increases for  $H_\gamma$ . Therefore, by varying both  $n_e$  and  $T_e$ , it is possible to find the crossing points of the two lines where the theoretical Stark broadening is equal to the experimental. The cross point represents the electron density and temperature of the system.

### 3.2.4 Langmuir Probe Theory

Langmuir probes are used to measure electron temperatures and plasma densities. The literature has shown various solutions for Langmuir probes operating in high pressure systems[115], [117], [118], [120], [129], [130]. In 1963, Su and Lam[115] published work on spherical probes (single Langmuir probes) within flames. This work was expanded and eventually modified for cylindrical probes[131], [132]. High pressure Single Langmuir probe (SLP) theory is divided into six regimes[129], which are governed by three nondimensional numbers: the electric Reynolds number ( $R_e$ ), a Debye ratio ( $\alpha$ ), and the probe bias voltage ( $\chi$ ). These are expressed as

$$R_e = \frac{2r_p v_f}{\mu_i T_{eV}}, \quad (3.13)$$

$$\alpha = \frac{\lambda_D}{r_p}, \quad (3.14)$$

$$\chi = \frac{V_p}{T_{eV}}, \quad (3.15)$$

where  $r_p$  is the probe radius,  $v_f$  is the bulk flow velocity,  $\mu_i$  is the ion mobility,  $T_{eV}$  is the electron temperature in units of eV,  $\lambda_D$  is the Debye length, and  $V_p$  is the probe bias voltage in volts.

### 3.3.1.1 Stationary Plasma Regimes

Two of the regimes cover stationary plasmas where  $Re < 1$ , or where ion measurement by the probe is primarily controlled by diffusion processes rather than flow convection. At low bias voltages, the probe sheath is thin with respect to the probe radius ( $\alpha\chi \ll 1$ )[133]. The radius of the sheath therefore can be approximated as the radius of the probe ( $r_{sheath} \approx r_p$ ), meaning the sheath has negligible effects on the current measurement[133]. As the bias voltage increases, the sheath grows and can begin to affect the ion collection area. When the sheath radius becomes much larger than that of the probe, at  $\alpha\chi \gg 1$  [118], the thin sheath equation leads to an over calculation of the density.

### 3.3.1.2 Flowing Plasma Regimes

In the presence of high pressures or gas velocities  $> 1$  m/s, the ion transport is typically accomplished through flow convection rather than diffusion ( $Re > 1$ ). Smy[129] classified flowing plasmas into three regimes: diffusion-convection, sheath-convection, and E-field-convection. The probe sheath thickness dictates which regime the system is operating in, as shown in Fig. 3.11. The diffusion-convection regime develops when the sheath thickness is small compared to the probe radius and is smaller than the boundary

layer. This regime occurs when  $R_e \alpha^2 \chi^2 \ll 1$ [129]. As the sheath thickness increases and becomes thicker than the boundary layer, there is a transition into the sheath-convection regime. This regime is split into two sub-regimes: thin and thick. The thin sheath-convection regime occurs when  $R_e \alpha^2 \chi^2 \gg 1$ ,  $R_e \alpha \chi^{-\frac{1}{2}} < 1$ , and  $\alpha \chi \ll 1$ [132]. The thick sheath-convection regime, characterized by when the sheath becomes significantly thicker than the probe and boundary layer, occurs when  $R_e \alpha^2 \chi^2 \gg 1$ ,  $R_e \alpha \chi^{-\frac{1}{2}} < 1$ , and  $\alpha \chi \gg 1$ [131]. The final regime, E-field-convection, occurs when the probe sheath thickness is much larger than the boundary layer and  $R_e \alpha \chi^{-\frac{1}{2}} > 1$ [134].

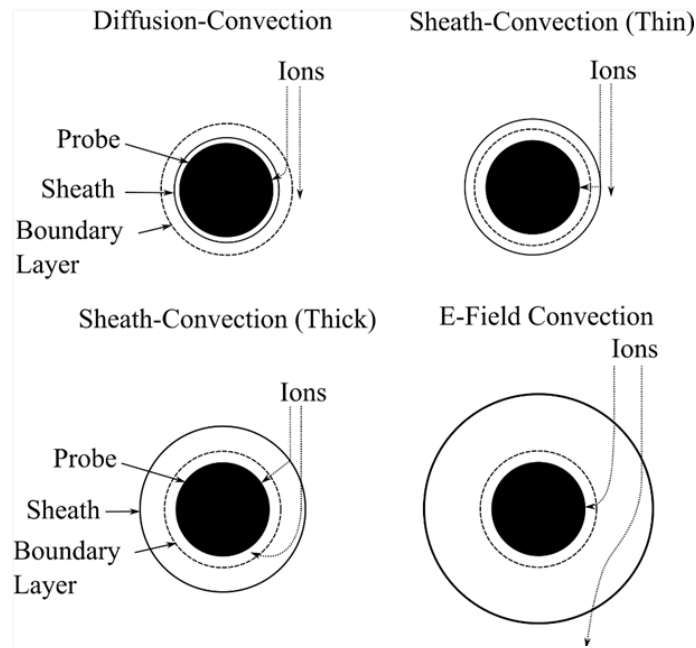


Figure 3.11 Drawings of flowing probe regimes.

### 3.3.1.3 Plasma Density Measurement

Based on the regime that the Langmuir probe is experiencing, the ion density can be calculated from the ion saturation current. A summary of the six regimes, their non-dimensional number criteria values, and their plasma density equations are shown in

Table 3.1. Details about variable notation and values can be found in the referenced literature.

Table 3.1 Plasma density solutions for the six high-pressure Langmuir probe regimes.

Plasma	Regime	Criteria	Plasma Density	References
Stationary	Thin sheath	$R_e < 1, \alpha\chi \ll 1$	$n_0 = \frac{I_{i,sat} \ln\left(\frac{\pi L}{4r_p}\right)}{2\pi L k \mu_i (T_e + T_i)}$	[133]
	Thick sheath	$R_e < 1, \alpha\chi \gg 1$	$n_0 = \frac{I_{i,sat} \ln\left(\frac{\pi L}{4r_p R_s}\right)}{2\pi L k \mu_i (T_e + T_i)}$	[118]
Flowing	Diffusion-convection	$R_e > 1,$ $R_e \alpha^2 \chi^2 \ll 1,$ $\alpha\chi \ll 1$	$n_0 = \frac{I_{i,sat}}{4L \sqrt{e \mu_i r_p v_f k T_e}}$	[116]
	Sheath-convection (thin)	$R_e > 1,$ $R_e \alpha^2 \chi^2 \gg 1,$ $R_e \alpha \chi^{-\frac{1}{2}} < 1,$ $\alpha\chi \ll 1$	$n_0 = \left[ \frac{I_{i,sat}}{5.3 (ev_f)^{\frac{3}{4}} (\epsilon_0 \mu_i r_p)^{\frac{1}{4}} V_p^{\frac{1}{2}} L} \right]^{\frac{4}{3}}$	[132]
	Sheath-convection (thick)	$R_e > 1,$ $R_e \alpha^2 \chi^2 \gg 1,$ $R_e \alpha \chi^{-\frac{1}{2}} < 1,$ $\alpha\chi \gg 1$	$n_0 = \frac{I_{i,sat}}{2L (\pi \mu_i \epsilon_0)^{\frac{1}{3}} (n_0 ev_f V_p)^{\frac{2}{3}} \left[ \log\left(\frac{I_{i,sat}}{2n_0 ev_f r_p}\right) \right]^{\frac{2}{3}}}$	[131]
	E field convection	$R_e > 1,$ $R_e \alpha \chi^{-\frac{1}{2}} > 1$	$n_0 = \frac{I_{i,sat} \epsilon_0^{0.3}}{5\pi e^{1.3} \mu_i V_p^{0.7} r_p^{0.6} L}$	[134]

For high pressure plasmas, the ion temperature can be assumed to equal the gas temperature due to the high collision rate and similar mass between ions and neutrals[51].

### 3.3.1.4 Double Probe Theory / Electron Temperature Determination

A double Langmuir probes (DLP) is a floating probe which can be used to measure the electron temperature of plasmas. Due to the fact that each probe filament is

referenced to the other, lower voltages are needed to reach saturation. In the case of symmetric double probes, such as those used in this work, the electron temperature can be obtained from the slope of the current-voltage (I-V) curve at zero current and the ion saturation current, or

$$T_{eV} = \frac{\frac{I_{i,sat}}{6.16}}{\left(\frac{dI_p}{dV_p}\right)_{t_p=0}}. \quad (3.16)$$

Due to symmetry,  $I_{i,sat}$  should be the same for both filaments, although in real world testing  $I_{i,sat}$  is often taken as the average of the two ion saturation currents.

## CHAPTER 4

### RESULTS

*Scientific research involves going beyond the well-trodden and well-tested ideas and theories that form the core of scientific knowledge. During the time scientists are working things out, some results will be right, and others will be wrong. Over time, the right results will emerge.*

- Lisa Randall

#### 4.1 Gas Temperature Determination

Experiments were performed on the AMPJ setup in two configurations: linear-field and cross-field. Four different methods were used to determine the gas temperature of the plasma: van der Waals broadening of argon spectral lines, spectral fitting of OH (A-X) and N<sub>2</sub> (C-B) spectra, and type K thermocouples.

##### 4.1.1 Comparison of Argon Broadening Components

In plasmas where the collisions between the natural and emitter species are frequent, the Stark broadening parameter can be neglected. As mentioned prior, this is often true for plasmas with relatively low gas temperatures and electron densities  $< 10^{16}$  cm<sup>-3</sup>. In order to verify the impact of neglecting this broadening parameter, sample calculations of broadening values for two argon lines were done for specific gas

temperatures, electron temperatures, and electron densities. Data from prior experiments with the linear-field configuration AMPJ[51] was used for the expected electron temperature and density. Eq. 2.7, which shows the simplified Stark broadening equation, can be used to solve the value of the Stark component for each line. The electron impact parameter,  $w$ , is tabulated for different temperatures given a fixed value for the electron density[121]. Therefore, as the electron temperature and density increases, the Stark broadening value increases. One can also see that the broadening is independent of the emission wavelength being analyzed.

Past experiments with the linear-field configuration AMPJ provided electron temperature and density values between 3.05 – 3.45 eV and  $5.0 \times 10^{10}$  –  $2.5 \times 10^{12}$  cm<sup>-3</sup>, respectively[51]. In order to simulate conditions where the Stark component would be at its maximum value, which corresponds to the point of the highest electron temperature and density, the values of 3.45 eV and  $2.5 \times 10^{12}$  cm<sup>-3</sup> were used.

The instrumental broadening component is also assumed independent of the emission wavelength being analyzed, thus remaining a constant 0.0992 nm. The Doppler and van der Waals broadening parameters are calculated from Eq. 2.1 and 2.2 for the assumed gas temperatures. Table 4.1 shows the results of this analysis for two different argon lines at gas temperatures of 300 and 400 K. The results show that the Stark component is two to three orders of magnitude smaller than the Doppler and van der Waals components. This confirms that it is acceptable to consider the Stark broadening parameter negligible for this microplasma jet.

Table 4.1 Broadening parameter values,  $T_e = 3.45$  eV,  $n_e = 2.5 \times 10^{12}$  cm<sup>-3</sup> (units of nm).

Argon Line	Gas Temperature (K)	Instrumental	Doppler	van der Waals	Stark
750.4	300	9.92E-2	1.45E-3	3.70E-2	3.32E-5
	400	9.92E-2	1.67E-3	3.02E-2	3.32E-5
696.5	300	9.92E-2	1.57E-3	3.97E-2	3.32E-5
	400	9.92E-2	1.81E-3	3.24E-2	3.32E-5

#### 4.1.2 OH (A-X) Spectra

An example of the measured OH (A-X) spectrum at a power level of 50 W under the linear-field configuration AMPJ can be seen in Fig. 4.1a. As the power level increases, two main regions show noticeable change. These regions correspond to two subsets of three peaks each, being centered at 307 (R<sub>2</sub>) and 308 (Q<sub>1</sub>) nm, respectively.

Fig. 4.1b shows this small but noticeable change of the 307 nm peaks.

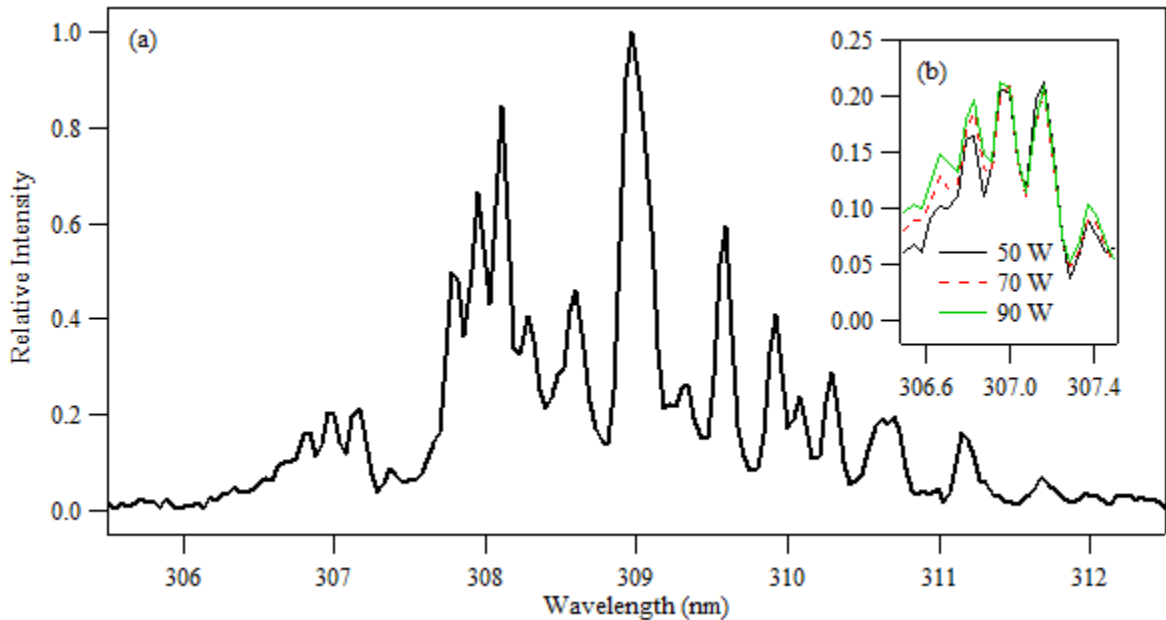


Figure 4.1 (a) OH (A-X) emission spectrum at 50 W for the linear-field configuration. (b) Variation on the emission spectra due to varying power levels, centered at 307 nm.

Each of the OH spectra were imported into both Specair and Lifbase. In order to obtain an accurate estimate of the gas temperature, the slit or instrument function must be accounted for. While Specair allows direct importing of the actual instrumental broadening data, Lifbase does not. Lifbase allows for the user to set the FWHM of the instrumental spectrum and provide the line shape. For the purposes of this study, the line shape was set to Gaussian and the measured instrument broadening FWHM was used in Lifbase. In Specair, the measured instrument function was imported into the simulation software.

Fig. 4.2 shows the results of the simulation analysis. Specair and Lifbase results for each configuration appear to agree to each other within the uncertainty for all power levels. The cross-field results are also higher than the linear-field, which is expected due to the immersion of the powered pin in the plasma for the cross-field configuration. The large error attributed to the Lifbase results is an artifact of the small difference in comparisons between two distinct peak groups, centered at 307 (R<sub>2</sub>, lines 8-10) and 308 (Q<sub>1</sub>, lines 1-3) nm. Depending upon which peak group is primarily considered as the basis of the temperature determination, the simulation software results in different temperature values.

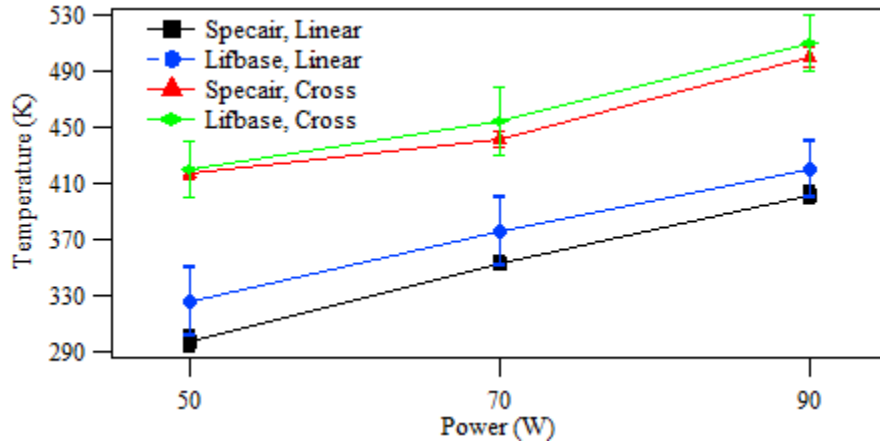


Figure 4.2 Gas temperature determination from OH (A-X) spectra comparison to Specair and Lifbase simulations.

The Specair simulation for the 50 W linear-field configuration is shown in Fig. 4.3a. The majority of the simulation peaks match the experimental data, yielding a final gas temperature of 297 K. The Lifbase simulation results are shown in Fig. 4.4. Figs. 4.4a and 4.4b show the results with priority given to the Q<sub>1</sub> (300 K) and R<sub>2</sub> (350 K) OH (A-X) peaks, respectively.

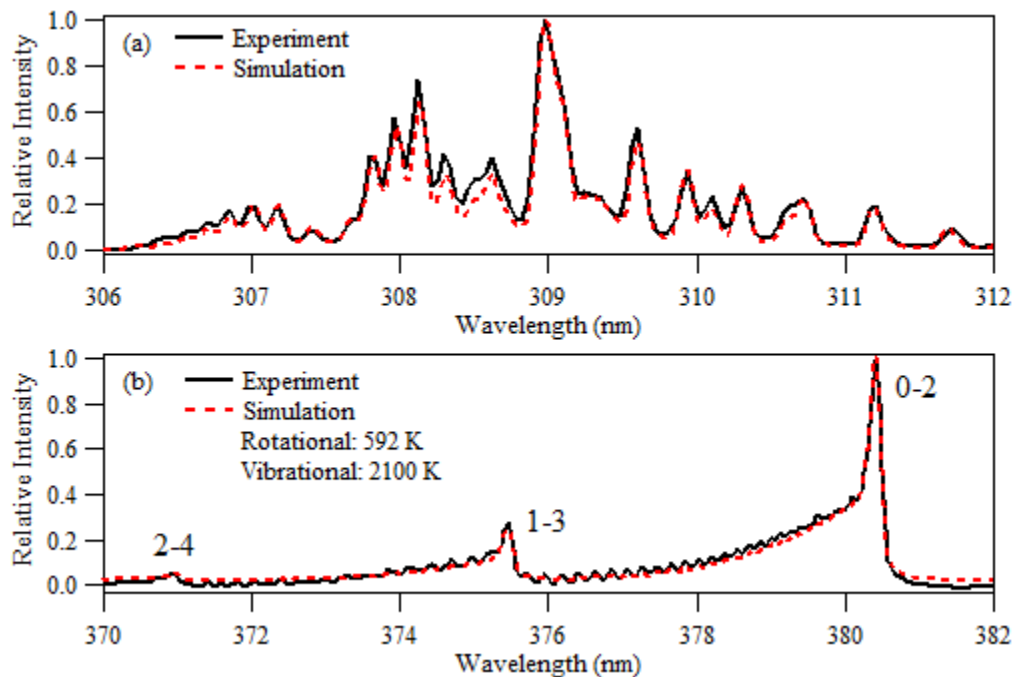


Figure 4.3 Specair simulation results for 50 W, linear-field configuration: (a) OH (A-X) and (b) N<sub>2</sub> (C-B),  $\Delta v = -2$ .

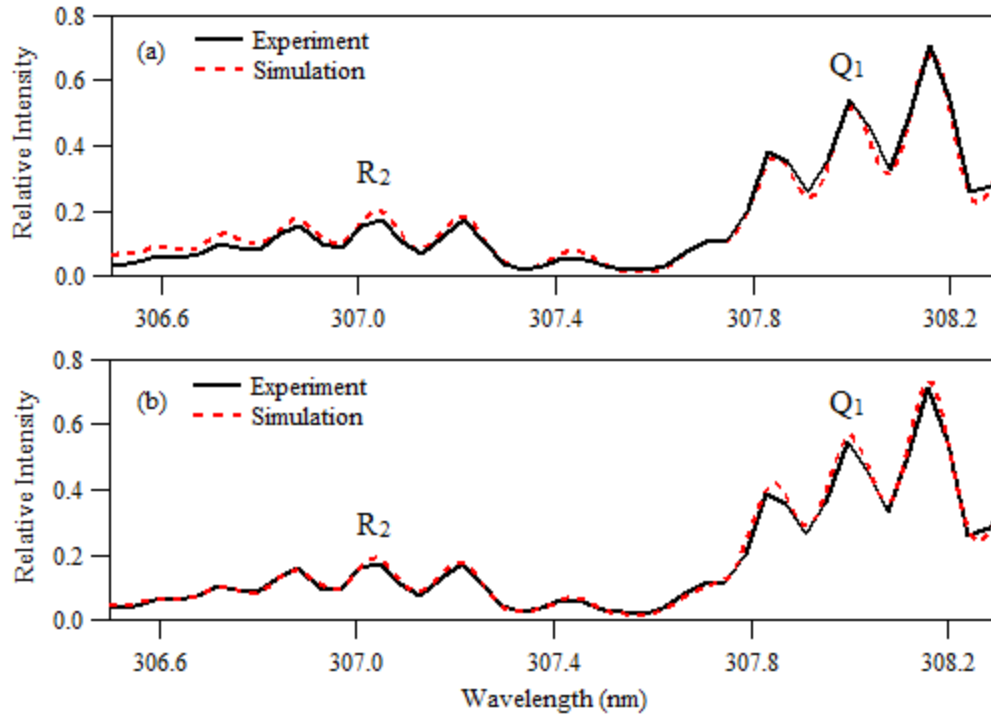


Figure 4.4 Lifbase simulation results for 50 W, linear-field configuration, OH (A-X): (a) priority given to Q<sub>1</sub> branch, (b) priority given to R<sub>2</sub> branch. The Q<sub>1</sub> branch resulted in a simulated temperature of 300 K, while the R<sub>2</sub> branch resulted in a simulated temperature of 350 K.

The difference in simulation results may be caused by the difference of the slit function input. Another factor to consider is that Lifbase does not provide automatic temperature determination. In other words, the user must set the temperature to test and determine visually if the experimental data matches. Lastly, as mentioned prior, the Lifbase results are dependent upon which peak set is primarily used for comparison. When prioritizing the Q<sub>1</sub> peaks, the temperature results for Lifbase are lower, matching very well to the Specair simulations. When focusing on the R<sub>2</sub> peaks, the Lifbase temperatures are higher and show more deviation from those of Specair. All of these contribute to small but noticeable differences between each simulation's results.

### 4.1.3 N<sub>2</sub> (C-B) Spectra

N<sub>2</sub> rotational lines with a  $\Delta v = -3, -2,$  and  $-1$  were captured with the optical emissions spectroscopy system. The N<sub>2</sub> (C-B) spectra at 70 W for the linear-field configuration is shown in Figs. 4.5a. Fig. 4.5b shows minor differences in the results for varying power levels at  $\Delta v = -3$ .

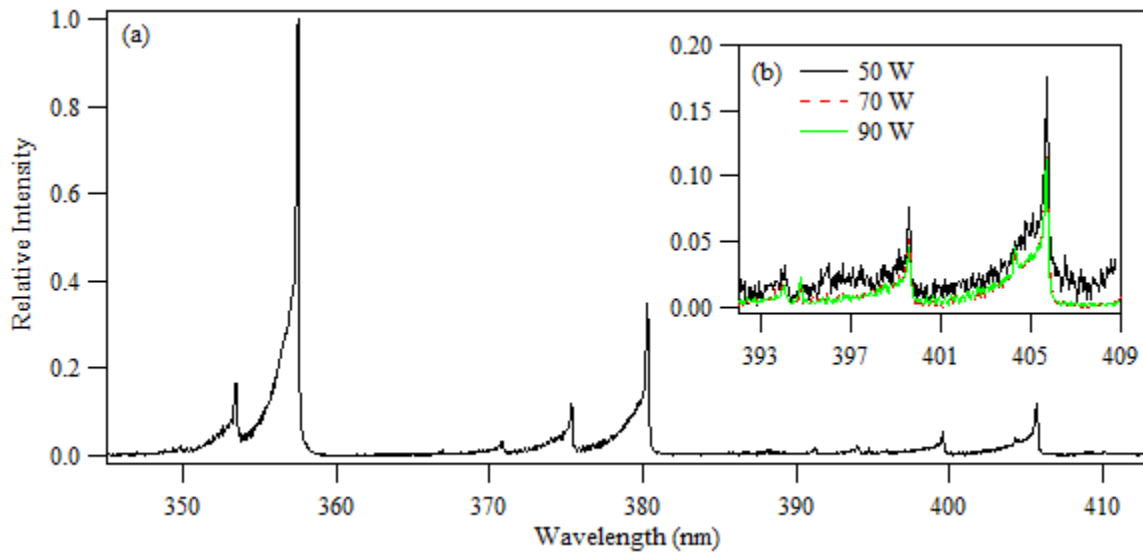


Figure 4.5 (a) N<sub>2</sub> (C-B) emission spectrum at 70 W for the linear-field configuration. (b) Variation on the emission spectra due to varying power levels, centered at 401 nm and showing the  $\Delta v = -3$  peak set.

Lifbase is not capable of simulating the second positive system of nitrogen, thus only Specair was used. The results of the analysis are shown in Fig. 4.6. As expected, the cross-field temperatures are higher than the linear-field.

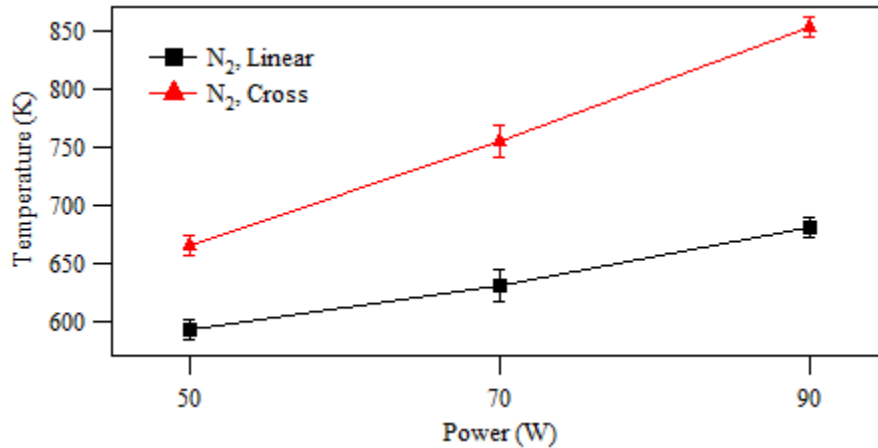


Figure 4.6 (a) Temperature determination from N<sub>2</sub> (C-B) spectra comparison to Specair simulations.

The Specair simulation for the 50 W linear-field configuration at  $\Delta\nu = -2$  is shown in Fig. 4.3b. The simulation appears to adequately capture the 0-2 transition and “finger” regions between the main peaks. There is a visible difference in the 1-3 and 2-4 peak intensities. This particular spectrum yielded a final gas temperature of 592 K.

#### 4.1.4 van der Waals Calculations of Argon (2p-1s)

In order to determine the gas temperature from van der Waals broadening techniques, individual argon emission lines were measured. The argon spectra at 50 W for the linear-field configuration are shown in Figs. 4.7a to 4.7c. Fig. 4.7d shows the variation of two argon emission lines, 800 and 801 nm, due to varying power levels for the linear-field configuration. While the change between lines in some cases is very small to the eye, it does impact the temperature calculation noticeably.

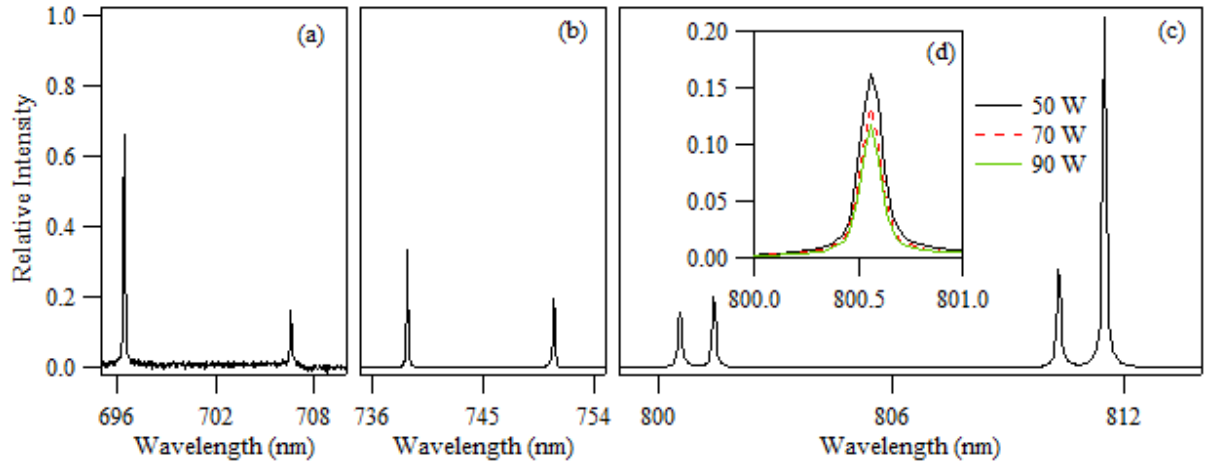


Figure 4.7 (a) 50 W argon spectra lines for the linear-field configuration: (a) 696 and 706 nm peaks, (b) 738 and 751 nm peaks, (c) 800, 801, 810, and 811 nm peaks. (d) The variation on the emission spectra due to varying power levels at 800 and 801 nm argon peaks.

Fig. 4.8 shows six argon lines (738, 751, 800, 810, 811, and 842 nm) that produced reasonable temperatures for the linear-field configuration. The other two lines (696 and 801 nm) provided non-realistic results that were either much too high ( $>1000$  K) or could not be calculated. This was due to an inability to obtain a good Voigt fit of the spectra. The specific grating angle affects how many measurements are taken for a given peak on the CCD. Error bar values were determined from a set of nine measurements at each data point. The 738, 800, and 810 nm argon lines appear to agree to each other within the uncertainty for all power levels. The 842 nm line yields elevated temperatures, but matches very well at 90 W. The 751 and 811 nm lines show elevated temperatures at all power levels.

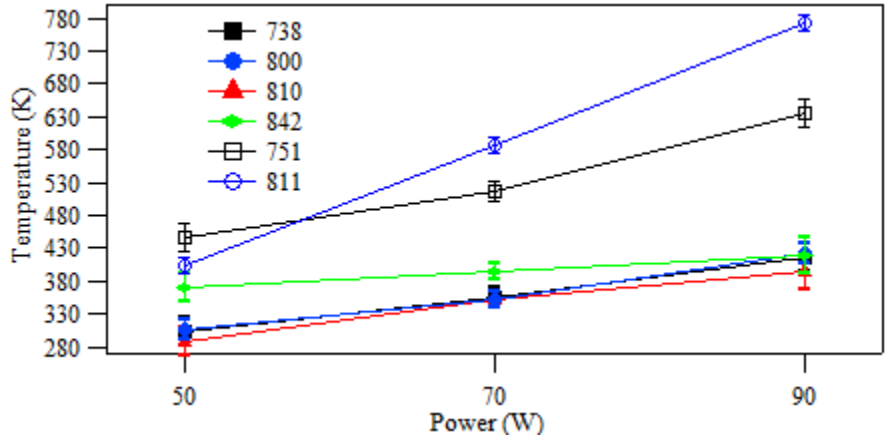


Figure 4.8 Temperature determination from van der Waals broadening of several argon spectral lines for the linear-field configuration.

Fig. 4.9 shows temperature measurements obtained for the cross-field configuration. Once again, the error bar values are based on a set of nine tests for each data point. The 738, 751, 800, and 810 nm lines appear to show similar groupings and trends across all power levels. The 842 nm line starts off roughly at the same temperature value at 50 W, but has drastically lower values at 70 and 90 W.

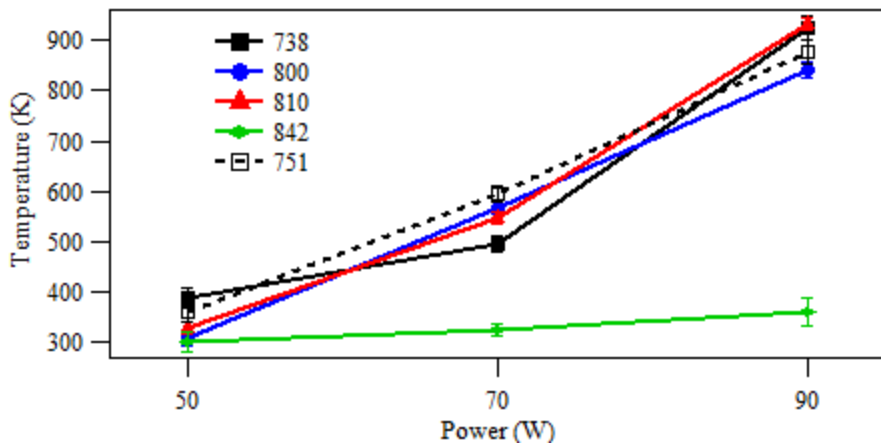


Figure 4.9 Temperature determination from van der Waals broadening of several argon spectral lines for the cross-field configuration.

### 4.1.5 Thermocouples

As previously mentioned, two type-K thermocouples were used as a cost effective method to directly obtain an estimate of the gas temperature. Due to arcing risks, only the adhesive thermocouple was used for the cross-field configuration. Fig. 4.10 shows the temperature results as a function of power. For the linear-field configuration, the shielded and adhesive T/Cs yield results within range of each other. The cross-field configuration results show an increase in temperature across all power levels. This is expected as the temperature is expected to increase for the cross-field plasma jet.

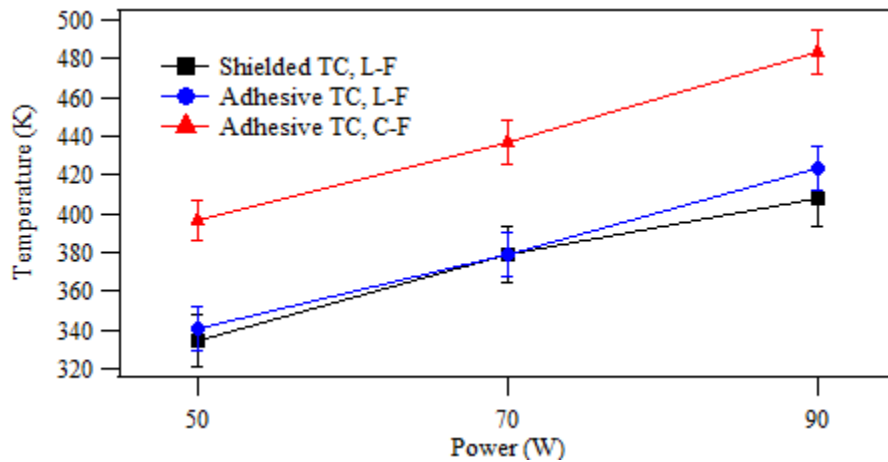


Figure 4.10 Temperature determination from two type-K thermocouples. L-F stands for linear-field, while C-F stands for cross-field.

### 4.1.6 Method Comparison

The results of the nitrogen simulations show drastically elevated temperatures in comparison to those of other gas determination methods, having values ranging from 593-850 K, depending on the configuration. The inaccuracy of the N<sub>2</sub> second positive system has been observed by others as well, especially for argon plasmas[58]. The cause

is an energy transfer from the  $\text{Ar}(^3\text{P}_{0,2})$  state via  $\text{Ar}(^3\text{P}_{0,2}) + \text{N}_2(\text{X}) \rightarrow \text{Ar}(^1\text{S}_0) + \text{N}_2(\text{C})$  [95]. This causes the rotational sublevel populations to deviate from a Boltzmann distribution, which in turn leads to inaccurate gas temperature measurements. Another reason for the inaccuracy of the second positive system is based on the location of the optical measurements in relation to the electric field being applied to the system. Due to the measurements taking place downstream of the applied electric field and in the emanating plasma jet, the electric field is lower. Popov[98] et al and Rusterholtz et al[93] have shown that in the presence of weak electric fields ( $E/N < 80$  Td), the  $\text{N}_2(\text{C-B})$  rotational distribution drastically changes and the gas temperature is overestimated. It is for these reasons that some studies recommend the utilization of the first positive system, which is less prone to errors. Unfortunately, the first positive system was not strong enough to be used in this work.

The results of the simulations are in better agreement to the argon and thermocouple results. Fig. 4.11a and 4.11b show this comparison for the linear-field and cross-field configurations, respectively. The simulation temperatures were similar for the van der Waals broadening method, regardless of the simulation software used. For the linear-field jet, the T/C temperatures matched well to the Lifbase OH results, but were elevated compared to Specair. For the cross-field jet though, the OH spectra and T/C values showed an extremely tight grouping, with values ranging from 393-510 K.

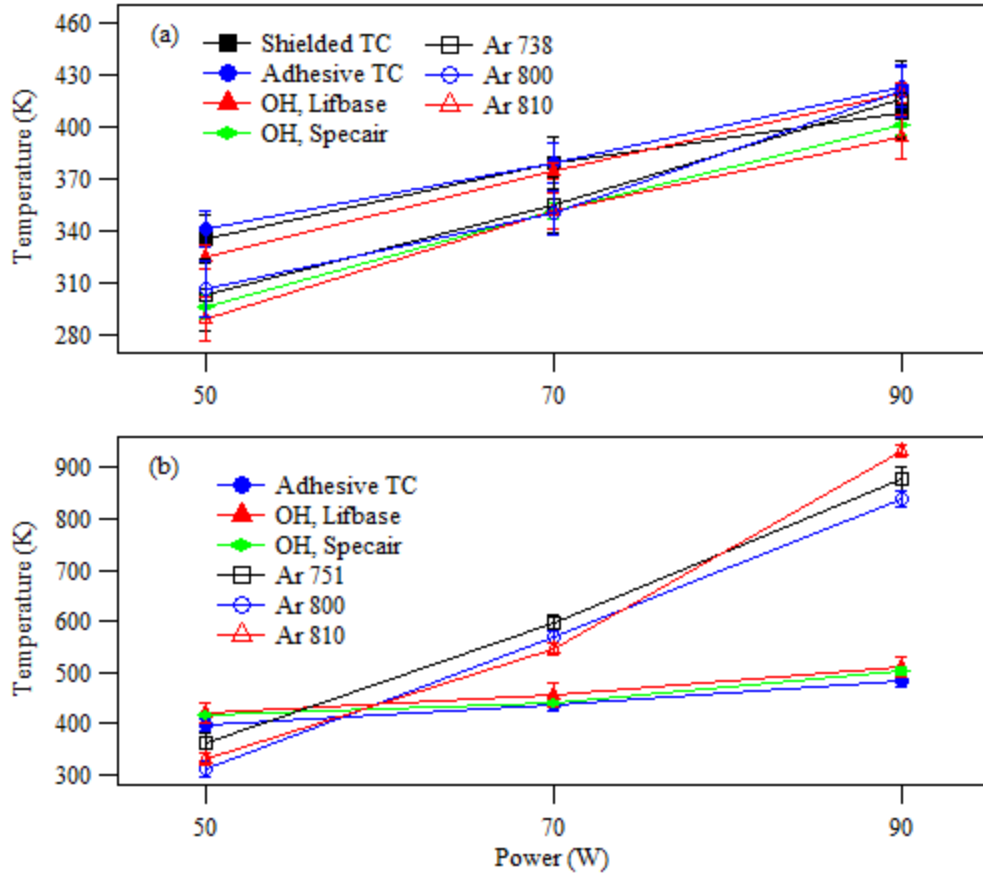


Figure 4.11 Temperature determination results for (a) linear-field jet and (b) cross-field jet, through multiple methods.

One can see that the individual argon lines exhibit different behavior depending on the configuration utilized and not all are accurate. A similar experiment was conducted with a high voltage pulsed dc AMPJ and showed different argon lines (696, 706, and 794 nm) matched OH and T/C temperatures compared to the rf AMPJ.

#### 4.2 Electron Temperature and Electron Density Determination

Due to the potential for arcing to the Langmuir probe filaments, only the cross-field configuration of the AMPJ was tested. Single and double Langmuir probes were utilized to determine these two properties.

### 4.2.1 Electron Temperature

The SLP plasma density equations require the electron temperature to be known. The ion temperature can be assumed to be equal to the gas temperature[51]. The electron temperature can be determined with a DLP by measuring the slope of the current-voltage (I-V) curve at zero current and the ion saturation current. The electron temperature was found for 50-90 W as a function of distance, as Langmuir probes can be used for spatial measurements. Fig. 4.12 shows this feature through I-V plots obtained at 70 W but with different distances. Fig. 4.13 shows the impact power also has on the resulting I-V plots.

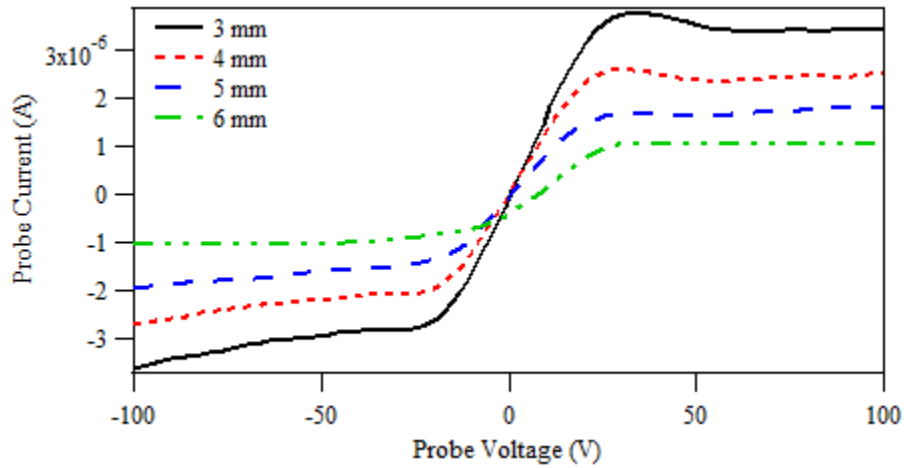


Figure 4.12 Double Langmuir probe I-V measurements at 70 W for various distances.

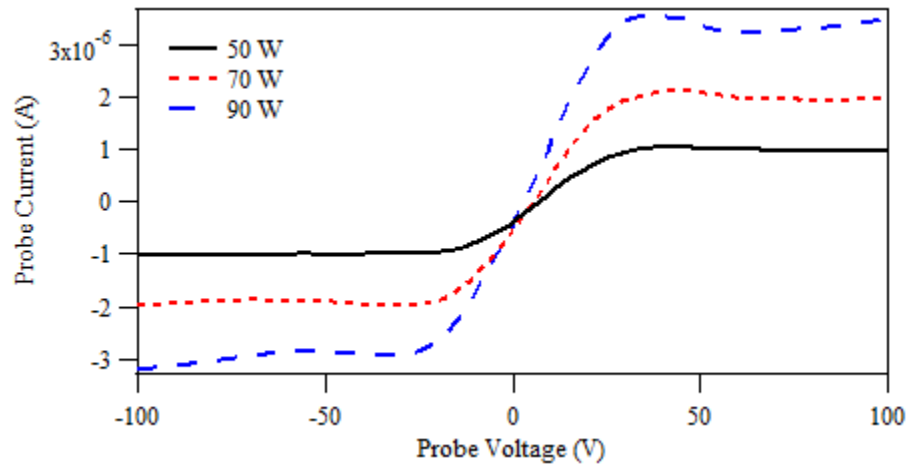


Figure 4.13 Double Langmuir probe I-V measurements at 5 mm for various powers.

The raw data was smoothed using a locally weighted scatter plot method before being analyzed. Precautions were taken to assure that the data was not significantly altered. Fig. 4.14 shows an example of the raw and smoothed data for an experimental test at 70 W. Nearly all plots generated had some form of near-linear current readings at 0 V, as shown in Fig. 4.14b, although this is removed through the use of the smoothing function. The cause of the anomaly at 0 V is thought to be caused by the sourcemeter switching from negative to positive voltages.

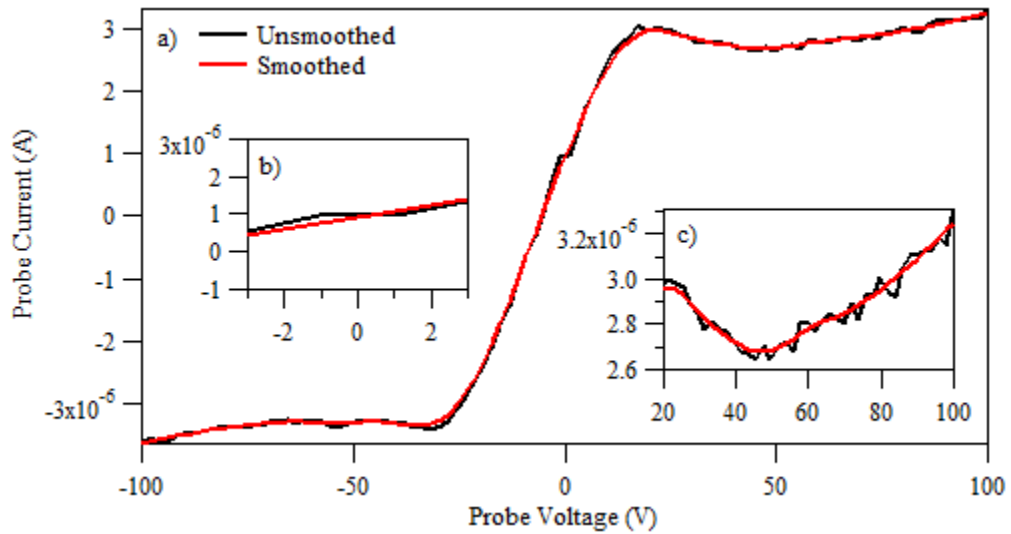


Figure 4.14 Comparison between raw and smoothed data.

The calculated electron temperatures as a function of distance are shown in Fig. 4.15. As the distance increases, the slope of the I-V curves at zero current decreases, which in turn yields higher electron temperatures. Based on prior experiments with this setup, an uncertainty of 15% was assumed due to uncertainty in the averaged data sets and the radial probe location[51]. Data points are omitted for the 90 W measurements at 2 mm due to arcing between the electrodes and the filaments.

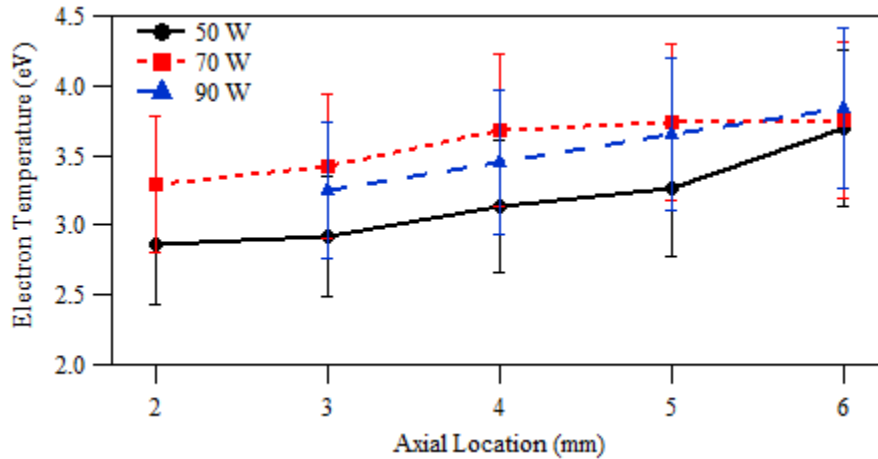


Figure 4.15 Electron temperatures as a function of location for 50-90 W with an uncertainty of  $\pm 15\%$ .

The electron temperature shows an increase with distance. 50 W showed the lowest temperature, being  $\sim 0.5$  eV less than the 70 and 90 W values. 90 W resulted in temperature values greater than those of 50 W, but slightly lower than those of 70 W. Prior studies have suggested that higher electron temperatures are obtained from faster recombination of low energy electrons within the jet. This may influence the results once a threshold power level is reached, such as  $> 50$  W, which would result in the 70 W temperatures being greater than those of 90 W.

#### 4.2.2 Electron Density and SLP Regimes

When using a SLP, the I-V curve shows a clear ion saturation region but has an improper electron saturation region, as shown in Fig. 4.16. The cause of this is a lack of a reference electrode, which leads to the continual growth of the sheath surrounding the probe with the bias voltage. With nowhere for ions repelled from the probe to go, the electron current continually increases. The central pin in the quartz tube is a ground

electrode, but is located just under 1 cm upstream of the probes. The mean-free-path of ion neutral collisions is  $\sim 0.04 \mu\text{m}$ [51], which is much less than the distance to the central pin. Based on SLP sweeps, the ion saturation is reached between -150 and -140 V. Therefore, the ion saturation value was chosen as the average of these values. For the regime calculations, a probe voltage of 145 V was used.

Various SLP probe regimes were tested to determine the correct plasma density of the plasma. The resulting probe regime criteria are shown in Table 4.2. All measurements were recorded in the flowing regime ( $Re > 1$ ), meaning the criteria  $Re \alpha^2 \chi^2 \ll 1$  places the probes in the diffusion-convection regime for all power levels and locations. Each potential regime has drastically different results, so it is important to carefully determine the regime criteria values. For example, at 50 W and 2 mm the plasma density is calculated as  $2.36 \times 10^{20} \text{ m}^{-3}$  with diffusion-convection,  $4.77 \times 10^{17} \text{ m}^{-3}$  (difference of 199%) with thin sheath-convection, and  $2.80 \times 10^{21} \text{ m}^{-3}$  (difference of 169%) with E-field convection. Three flowing plasma regimes as a function of probe location at 70 W are shown in Fig. 4.16. The inherent uncertainty of the sheath-convection solution is greater than  $\pm 30\%$ [51], [131].

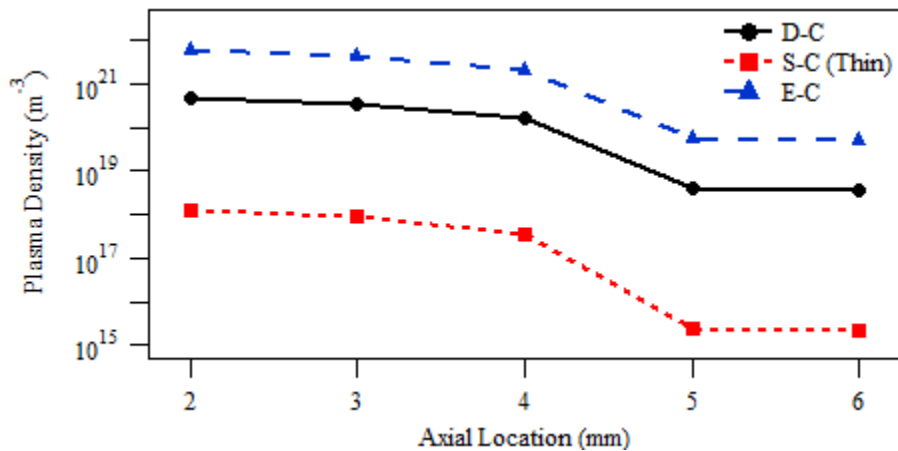


Figure 4.16 Flowing plasma regimes as a function of probe location at 70 W.

Table 4.2 Probe regime criteria values for ion saturation at -145 V; D-C stands for Diffusion-Convection.

Power (W)	Distance (mm)	$I_{sat}$ (A)	$T_{ev}$	$R_e$	$\alpha\chi$	$R_e\alpha^2\chi^2$	Regime
50	2	-1.02E-06	2.858	1.361	6.07E-03	5.01E-05	D-C
	3	-8.69E-07	2.914	1.335	6.54E-03	5.71E-05	D-C
	4	-6.36E-07	3.140	1.239	7.50E-03	6.97E-05	D-C
	5	-1.02E-08	3.269	1.190	5.87E-02	4.09E-03	D-C
	6	-6.90E-09	3.689	1.054	6.92E-02	5.05E-03	D-C
70	2	-2.11E-06	3.289	1.182	4.07E-03	1.96E-05	D-C
	3	-1.61E-06	3.425	1.135	4.61E-03	2.42E-05	D-C
	4	-7.84E-07	3.688	1.055	6.49E-03	4.44E-05	D-C
	5	-2.00E-08	3.732	1.042	4.05E-02	1.71E-03	D-C
	6	-1.81E-08	3.748	1.038	4.26E-02	1.88E-03	D-C
90	3	-1.70E-06	3.245	1.199	4.55E-03	2.48E-05	D-C
	4	-1.07E-06	3.444	1.129	5.65E-03	3.61E-05	D-C
	5	-3.31E-08	3.653	1.065	3.17E-02	1.07E-03	D-C
	6	-3.17E-08	3.834	1.014	3.20E-02	1.04E-03	D-C

Fig. 4.17 plots the plasma densities, according to the appropriate regimes, as a function of axial location with curves of power. Once again, data points are omitted for the 90 W measurements at 2 mm due to arcing between the electrodes and the filaments. There is a decrease in density with distance as expected. A drastic decrease in plasma density was observed for the transition between 4 and 5 mm, although the reason for this behavior is not known. Experimental uncertainties were determined by comparing the density from the three raw I-V curves with the final averaged density. Since the experimental uncertainty was found to be less than 30% for all operating conditions, the larger 30% proposed by Clements[131] is used.

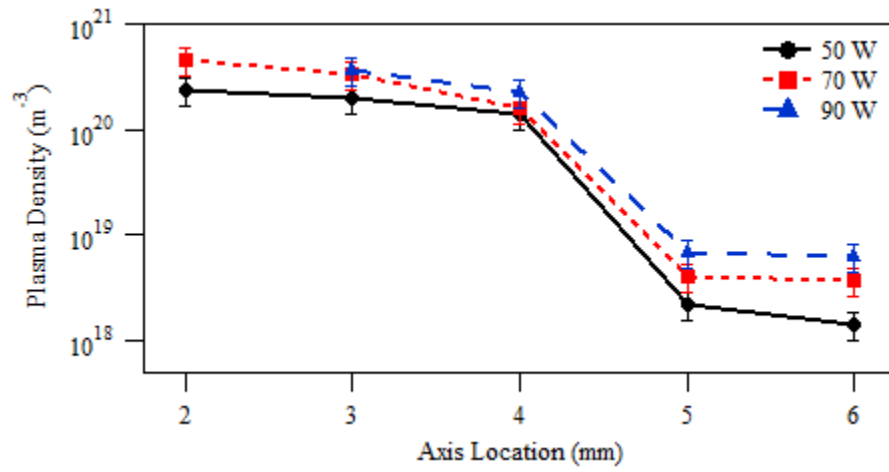


Figure 4.17 Plasma densities as a function of distance for powers between 50-90 W. All data was collected for the diffusion-convection regime.

## CHAPTER 5

### DISCUSSION

*Nothing in life is to be feared, it is only to be understood. Now is the time to understand more, so that we may fear less.*

- Marie Curie

#### 5.1 Gas Temperature

The cross-field jet yielded much higher temperatures from the argon lines. This can be due to the sensitivity of the spectrometer and the change in van der Waals broadening with temperature. The cross-field jet is expected to produce higher gas temperatures due to a direct contact between the powered electrode and the plasma. With assumption that the Stark and instrumental broadening remain constant over the change in gas temperature, the changing broadening of the emission line can be directly attributed to the variation in the Doppler and van der Waals components. As shown in Fig. 4.12, an increase in the gas temperature results in a decrease of the van der Waals value and an increase of the Doppler value. At low temperatures, due to the higher order of magnitude for the van der Waals broadening, the convoluted sum of the two decrease. At temperatures much higher than the crossing point of the two broadening parameters around 1200 K, an increase in temperature will result in a net increase in the sum due to the increasing Doppler component. The AMPJ in this work operates in the range of 300-

500 K, meaning that only a decrease in the sum is observed. Indeed, the higher temperature cross-field jet had an overall smaller broadening than the colder linear-field jet. This decrease in broadening is important as smaller values can cause larger errors due to the fact the method subtracts small numbers from small numbers. Thus lower van der Waals values will result in the temperature measurement with more uncertainty, for a given spectrometer resolution. Therefore, the use of van der Waals for gas temperature may be invalid for higher temperature systems.

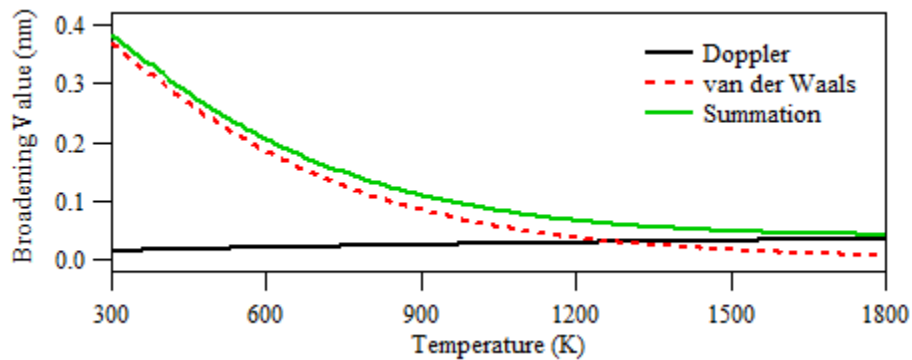


Figure 5.1 Doppler and van der Waals broadening values as a function of temperature for the 738 nm argon line. For the range of expected temperatures (300-500 K), the total broadening of argon lines will decrease as the temperature increases.

Boltzmann plots were initially generated for the OH (A-X) and N<sub>2</sub> (C-B) ( $\Delta v = -2$ ) spectra at 50 W, resulting in linear plots for both species as shown in Fig. 5.2. The methodology used to generate these plots, as well as sample calculations, is shown in Appendix B. While it is possible to measure the gas temperature from the slope of the graphs, it is best practice to utilize the spectral fits generated from simulation software, assuming a linear Boltzmann plot is observed, as it is more accurate. With that said, the OH (A-X) plots yielded temperatures of 449.5 K and 470.6 K for the linear-field and cross-field configurations, respectively. The N<sub>2</sub> (C-B) plots yielded temperatures of 499.7 K and 537.1 K for the linear-field and cross-field configurations, respectively.

Temperatures were found to be elevated in comparison to the other optical and physical probe measurements, although the linear plots indicated a Boltzmann population distribution behavior. After further inspection of the OH (A-X) and N<sub>2</sub> (C-B) spectra though, it was determined that they were not resolved enough to accurately apply Boltzmann plot analysis. Fig 5.3 shows an example comparison between experimental and simulated spectra for OH (A-X). Based on the comparison, we observed that several individual bands are being resolved together into one at some locations. Therefore the results can be misleading as multiple lines may be influencing the measured intensity. While experimental settings can be modified to improve resolution, it was determined that an equipment limitation had been reached. Therefore, Boltzmann plot analysis of these species has been omitted from this study. Improved equipment or better diagnostic settings should yield acceptable resolved spectra.

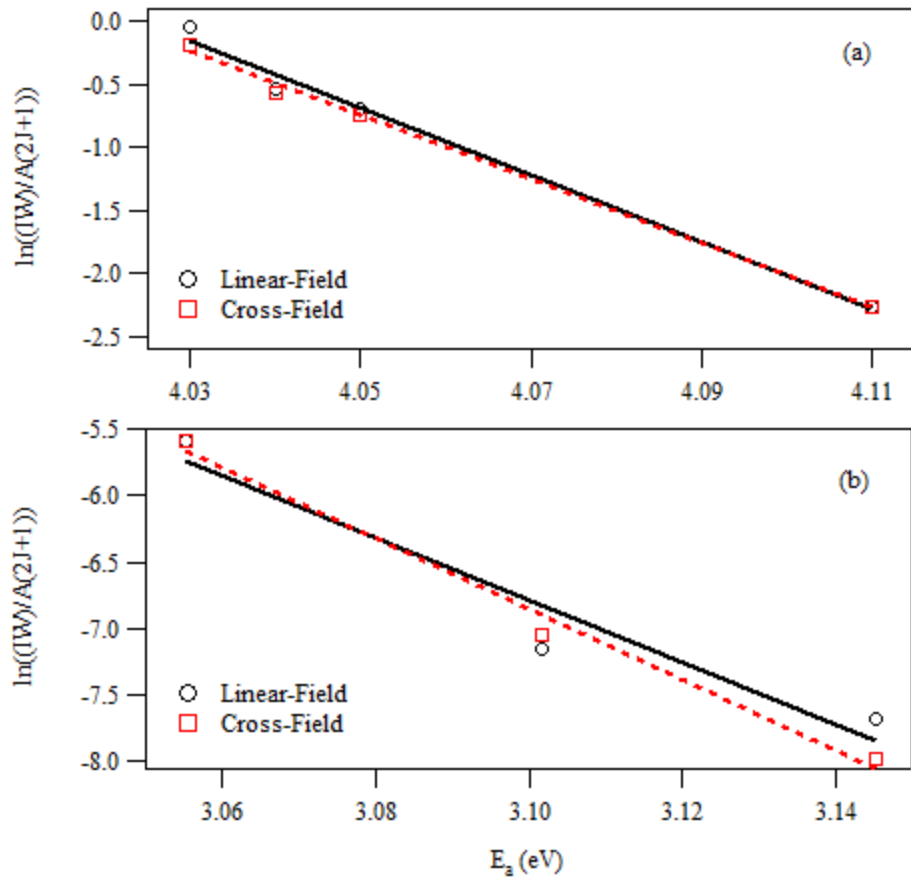


Figure 5.2 Sample Boltzmann plot generated for: (a) OH (A-X) and (b) N<sub>2</sub> (C-B).

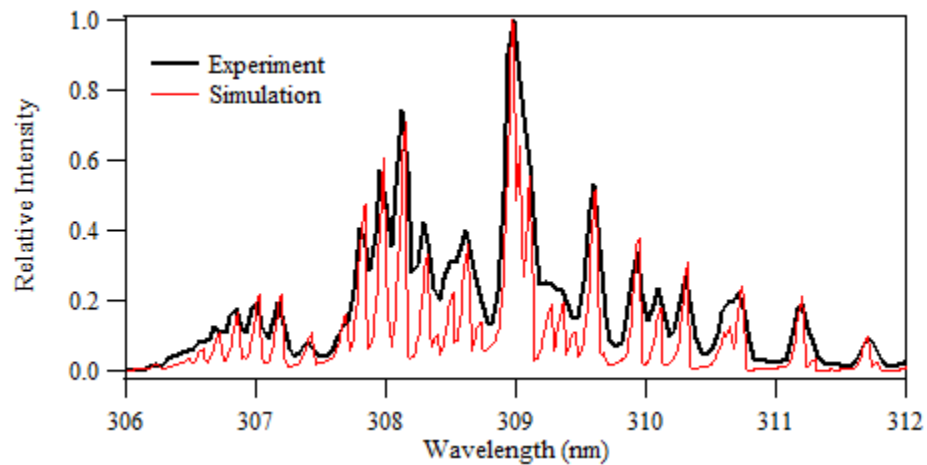


Figure 5.3 Sample comparison of experimental and simulated OH (A-X) spectra, highlighting a lack of resolution in the experimental data.

Due to rf interference from the power source, thermocouple readings were captured after turning off the power supply. While being the most cost-effective means of measuring gas temperature, careful consideration must be taken when using thermocouples. The use of tin foil wrapped around wires and leads from both the power supply and the thermocouple reader yielded lower interference levels, although some interference remained. Grounding the thermocouple reader also helped reduce some of this feedback.

Lastly, the use of van der Waals broadening of other gases such as hydrogen was considered. Unfortunately, as will be discussed in the next section, the hydrogen lines were not resolved completely. This resulted in unrealistic temperature measurements greater than 2000 K. A low vacuum setup was utilized in order to see if the atmospheric pressure condition was negatively impacting the line measurements. Even at low pressures ( $< 1$  torr), the lines remained unresolved. Various combinations of settings on the spectrometer and camera were tested, although the same issue persisted. Many studies have utilized hydrogen emission lines, leading to the conclusion that an equipment limitation with the optical emission spectroscopy system is present. Helium was also considered, although the gas was not readily available for testing during the time of the experiments. Additionally, resonance broadening is often included as a major broadening component, although the literature provides detailed instructions on its calculation.

## **5.2 Electron Temperature and Density**

The results indicate that density decreases with distance while electron temperature increases with distance. As observed in Fig. 5.4, all lines show clear

saturation and a consistent intersection. The slope at zero current,  $dI_p/dV_p$ , which is used for the electron temperature determination, is shallowest for larger distances. Therefore, larger temperatures are produced even though the saturation ion current value is slightly less. Larger temperatures in turn lead to smaller density values. The trends observed for both properties are correct.

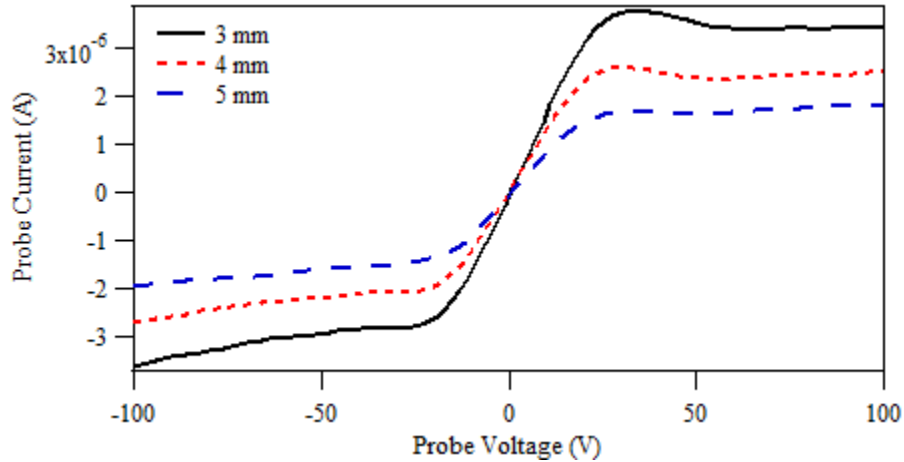


Figure 5.4 Example of DLP data for 70 W at various distances.

The observed trends may also be due to atmospheric-pressure operation; specifically mixing with ambient air. This can increase electron depletion via neutralization or increase diffusion[51]. The jet Reynolds number can be used to characterize the plume, which is

$$Re_{jet} = \frac{\rho v_f d}{\mu}, \quad (5.1)$$

where  $\rho$  is the density,  $v_f$  is the velocity,  $d$  is the diameter of the quartz tube, and  $\mu$  is the dynamic viscosity. At 2 slm, the jet Reynolds number is equal to 1119. Mixing between the jet and ambient air increase with increasing jet Reynolds number. Work by Labus[135] has shown that momentum loss due to mixing becomes significant at  $Re_{jet} >$

1000-1500. The increase in collisions can also deplete the low energy electrons[51]. This mixing can also yield additional molecular species which can affect the plasma chemistry of the jet. In addition to OH and N<sub>2</sub>, ozone and atomic oxygen[136] have also been observed in the jet even when using pure gas.

One issue with using Langmuir probes with AMPJs is the small size of the emitting plume. In the experiments performed in this study, the probe diameter and length are 4.1% and 66% of the diameter of the microplasma jet. At the low Reynolds numbers tested,  $\approx 48$ , the cylindrical probe should not significantly disturb the flow. According to Schlichting and Gersten[137], turbulent separation for a jet typically occurs at Reynolds numbers  $> 90$ . The 2 mm length of the probe and the 3 mm ID of the quartz tube means that the probe may not always be completely immersed within the plasma, especially at farther axial distances. Thus, different probe sections of the probes may see different regions of the plasma. Large probe lengths can lead to elevated electron temperatures since the low energy electrons are collected first. While this contributes to the uncertainty in the measurements, the observed trends remain intact.

An additional issue with using physical probes in general is the risk of arcing occurring between the probe and the electrode. This can cause perturbations, which are subsequently detected in the rf power and SWR readings. Due to the potential for arcing, careful consideration was taken when determining the useful range of distances for the probes. It is for this reason also that some data points are omitted in the results. In the event of arcing, readings returned to normal after removing the probe from the emanating jet.

The use of hydrogen Stark broadening was initially investigated as a potential optical method to verify the electron temperature and density. Stark broadening makes use of Balmer series lines of hydrogen; specifically  $H_\alpha$  (656.3 nm),  $H_\beta$  (486.1 nm), and  $H_\gamma$  (434.1 nm). Sample spectra obtained for these emissions lines are shown in Fig. 5.5.  $H_\gamma$ , shown in Fig. 5.5c, could not be resolved from the spectra observed, in part due to a significant amount of noise with respect to the few identifiable emission lines. The  $H_\beta$  spectra, shown in Fig. 5.5b, yielded inconclusive results. Due to atmospheric operation, species other than argon are present. Therefore, it is unknown whether the observed peak is definitively  $H_\beta$ . The peak was analyzed and the Stark broadening value was back-calculated from the measured Voigt fit. Unfortunately, the Stark broadening was determined to be negative (physically impossible), indicating that the line was not sufficiently resolved. The conditions required to make the contribution positive were found to be unrealistic for the system. Due to the density of the plasma ( $\sim 10^{14} \text{ cm}^{-3}$ ), the Stark contribution is extremely small, on the order of  $10^{-5}$ , meaning a higher resolution spectrometer is required to be able to accurately use the line. The  $H_\alpha$  spectra, shown in Fig. 5.5a, also led to inconclusive results. Other species have lines relatively close to  $H_\alpha$ , meaning that some lines may be combining or providing false peaks. A better resolution spectrometer would help correct this and possibly completely separate out the individual lines.

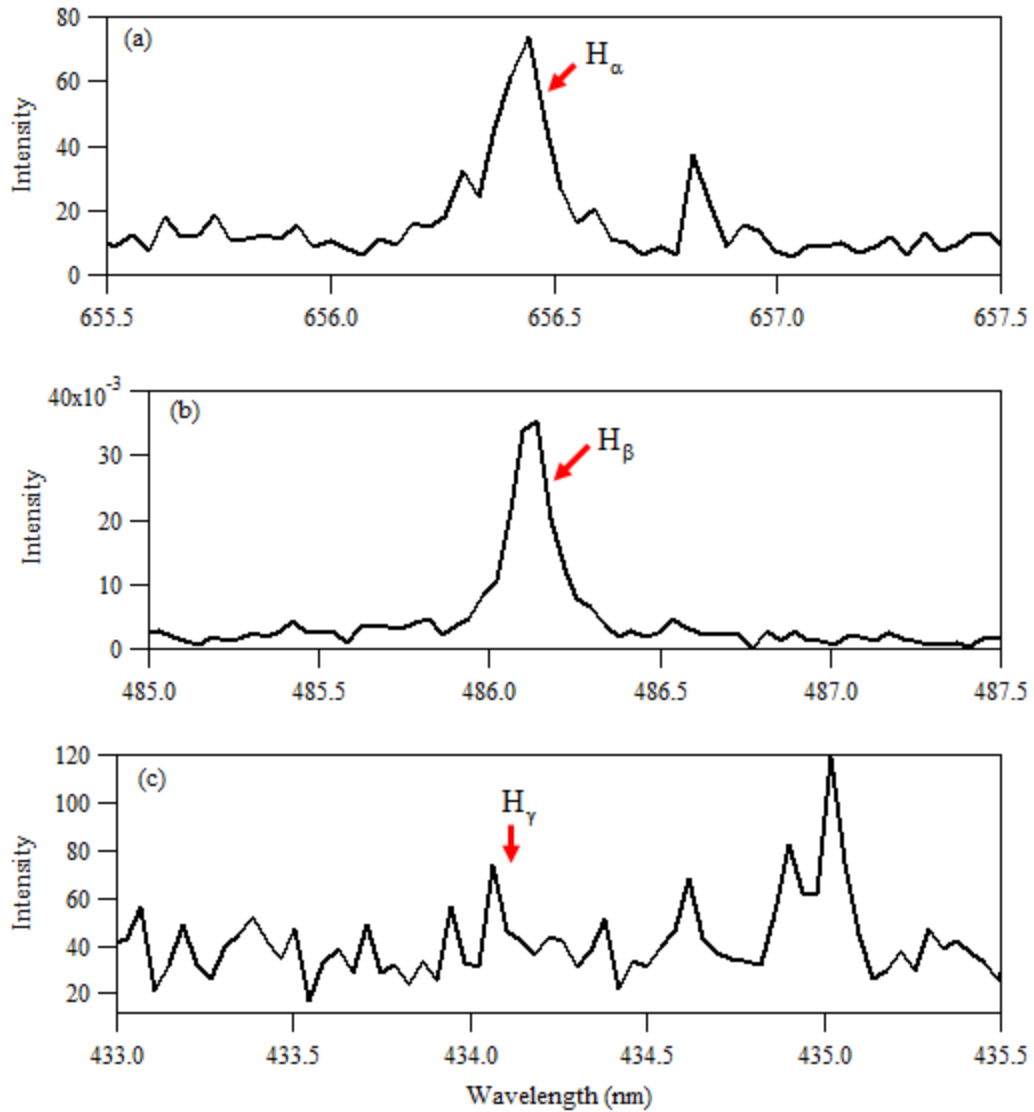


Figure 5.5 Sample spectra obtained for: (a) H $\alpha$ , (b) H $\beta$ , and (c) H $\gamma$

### 5.3 Comparison to Literature

Similar experimental configurations have been utilized in the literature. Those of interest have rf power sources and utilize a two electrode pin-tube geometry. Direct comparisons are hard to make as experimental factors such as gas flow rate, power settings, and others can impact the plasma properties.

Hofmann *et al*[56] used a tungsten needle and a 1.5 mm ID glass tube. The frequency was set at 11.66 MHz and argon was the plasma forming gas. The group used Rayleigh scattering as the standard temperature measurement due to its accuracy. Stark broadening of hydrogen was used to find the electron density only. The expected density range was known based on prior experiments. Therefore, a simplified Stark broadening equation was used to back-calculate the density. The equations utilize a double and single peak fit for H $\alpha$  and H $\beta$ , respectively, represented by

$$\Delta\lambda_{S,\alpha} = 1.78 * \left(\frac{n_e}{10^{23}}\right)^{\frac{2}{3}}, \quad (5.2)$$

$$\Delta\lambda_{S,\alpha} = 3.67 * \left(\frac{n_e}{10^{23}}\right)^{\frac{2}{3}}. \quad (5.3)$$

Gas temperatures and electron densities ranged from 375-540 K and  $2 \times 10^{19}$ - $1 \times 10^{20}$ , respectively.

Benedikt *et al*[14] used a 1 mm ID ceramic tube with a steel capillary powered at 13.56 MHz. The group used OH rotational bands for gas temperature measurements and Stark broadening of hydrogen for electron density. The gas temperature and electron density were measured as  $350 \pm 50$  K and  $8.5 \times 10^{20} \text{ m}^{-3}$ , respectively. No electron temperature value was provided in this study.

Xu and Doyle[51] used an identical experimental configuration, aside from the quartz tube diameter, which was set at 2 mm ID. Flow rates and power were varied from 0.5-2.0 slm and 30-90 W, respectively. Electron temperatures ranged from  $\sim 3.0$ - $4.3$  eV and densities were calculated between  $\sim 10^{16}$ - $10^{18} \text{ m}^{-3}$ . Due to the smaller diameter tube, the velocity of the gas flow at 2 slm was greater. This in turn affected the three dimensional numbers ( $R_e$ ,  $\alpha$ , and  $\chi$ ), which placed the probes in the sheath-convection

regime, which yields lower density values than those of the diffusion-convection regime. There is typically an order of  $10^2$ - $10^3$  difference between the regime values, which would account for the  $10^2$ - $10^3$  difference observed between the studies. The trends associated with the temperature and density values with respect to distance were identical.

## CHAPTER 6

### CONCLUSION

*A thinker sees his own actions as experiments and questions—as attempts to find out something. Success and failure are for him answers above all.*

- Friedrich Nietzsche

Optical methods and physical probes were used on an atmospheric microplasma jet to investigate the accuracy of gas temperature, electron temperature, and electron density measurements. Two AMPJ configurations, linear-field and cross-field, were tested. Different optical techniques and probes were utilized to better understand their efficacy and accuracy when applied to AMPJs.

#### **6.1 Gas Temperature**

The OH spectra yielded the most consistent temperatures and can be considered the baseline for comparison. The results indicate that there is a noticeable difference in not only each of the different gas temperature determination methods, but also for individual argon spectral lines when using van der Waals broadening. In addition, the usefulness of argon spectra lines as a gas temperature measurement appears to vary with electrode configurations and temperatures.

Thus while van der Waals broadening is relatively easy to implement, careful consideration must be made when choosing the spectral lines. The resolution of the spectrometer system may also play a role in the accuracy of the line broadening method as the method uses very small numbers that can be strongly impacted by small uncertainty. A comparison measurement should be done to ensure the accuracy of the chosen argon lines for any given microplasma device.

The T/C yielded surprisingly accurate, if slightly elevated temperatures compared to the OH results; <13% for the linear-field configuration, and <5% for the cross-field configuration. Thermocouples thus may be considered a viable option to reliably estimate the microplasma gas temperatures, as long as proper shielding between the plasma and T/C is provided. A thin ceramic coating or sleeve such as those used for harsh environment T/Cs may provide sufficient insulation for these low temperatures and still allow fast response times.

## **6.2 Electron Temperature and Electron Density**

Langmuir probes have successfully been used to perform spatially resolved measurements of both the electron temperature and density. The electron temperature increases with distance, with 70 W yielding the highest temperatures. This behavior may be due to high collisionality which depletes low energy electrons via neutralization collisions as well as continuum flow turbulence that increase the loss of low energy electrons from mixing with cold ambient air. Plasma density decreases with distance, with the maximum occurring at 90 W. A sharp decrease was observed at the transition from a distance of 4 to 5 mm, although the reason is not known at this time. Results

indicate that the plasma properties can be adjusted by varying not only the power, but also the distance. While the use of Langmuir probes for atmospheric-pressure microplasma is hopeful, questions remain about their accuracy and the amount of perturbation to the plasma.

### **6.3 Future Work**

Many experiments found in the literature utilize Stark broadening of hydrogen emission lines. Due to what is believed to be an equipment limitation, the hydrogen lines were not well resolved. Additionally, the plasma densities measured by the Langmuir probe is near the lower density limit for detectable Stark broadening. Future work will focus on modifying the experimental setup so Stark broadening can accurately be measured. The goal is to compare the physical probe measurements obtained with Langmuir probes to optical methods, such as Stark broadening. The equipment modification should also result in better resolution of both N<sub>2</sub> and OH spectra, allow for Boltzmann plots to be used to determine the gas temperature.

Additional testing is also needed to determine the dependence on the use of individual ArI lines for gas temperature measurement with respect to AMPJ configuration. No literature has been found which explains in detail the cause of multiple argon neutral lines resulting in different gas temperature measurements.

Other diagnostic techniques such as Thompson and Rayleigh scattering and laser interferometry may be beneficial to pursue as additional plasma property determination methods. Thompson scattering would provide another method for electron density and

temperature measurements. Rayleigh scattering is often regarded as a very accurate gas temperature technique and therefore is an important topic to pursue.

Finally, the literature suggests that other species such as helium and the first positive and negative systems of  $N_2$  can also be used to measure the gas temperature and electron properties. With an upgrade of optical equipment and the addition of helium, these species can be analyzed. This would allow for the comparison of several additional optical methods to determine which can accurately be applied to AMPJs.

## APPENDIX A

### Argon Line Transition Probabilities and Energies

Table A.1 Argon Line Transition Probabilities and Energies.

Wavelength (nm)	Process	Einstein Coefficient ( $s^{-1}$ )	Lower Energy (eV)	Upper Energy (eV)	$R^2$ ( $cm^2$ )
696.5	$Ar(2p_2) \rightarrow Ar(1s_5) + h\nu$	$6.4 \times 10^6$	11.548	13.328	$4.62 \times 10^{-15}$
738.4	$Ar(2p_3) \rightarrow Ar(1s_4) + h\nu$	$8.7 \times 10^6$	11.624	13.302	$9.53 \times 10^{-16}$
706.7	$Ar(2p_3) \rightarrow Ar(1s_5) + h\nu$	$3.8 \times 10^6$	11.548	13.302	$9.81 \times 10^{-16}$
751.5	$Ar(2p_3) \rightarrow Ar(1s_4) + h\nu$	$4.0 \times 10^7$	11.624	13.273	$9.08 \times 10^{-16}$
800.6	$Ar(2p_5) \rightarrow Ar(1s_4) + h\nu$	$4.9 \times 10^6$	11.624	13.172	$7.62 \times 10^{-16}$
810.4	$Ar(2p_7) \rightarrow Ar(1s_4) + h\nu$	$2.5 \times 10^7$	11.624	13.153	$7.37 \times 10^{-16}$
842.5	$Ar(2p_8) \rightarrow Ar(1s_4) + h\nu$	$2.2 \times 10^7$	11.624	13.095	$6.63 \times 10^{-16}$
811.5	$Ar(2p_9) \rightarrow Ar(1s_5) + h\nu$	$3.3 \times 10^7$	11.548	13.076	$6.67 \times 10^{-16}$

## APPENDIX B

### Boltzmann Plots

Boltzmann plots were generated by plotting  $\ln[I_{rel}\lambda_{JJ'}/A_{JJ'}(2J + 1)]$  versus  $E_J$  for multiple OH (A-X) and N<sub>2</sub> (C-B) bands/transitions. Table B.1 shows the wavelength, Einstein coefficient, and energy of the utilized emission lines. The temperature can be calculated by  $T_g = -m_{slope}k$ , where  $k$  is the Boltzmann constant and  $m_{slope}$  is the slope of the plot. Sample calculations for the OH (A-X) spectra are shown in Tables B.2 and B.3.

Table B.1 Boltzmann plot spectra information.

Species	Band/Transition	Wavelength (nm)	A (s <sup>-1</sup> )	Energy (eV)
OH (A-X) Q <sub>1</sub> (0,0)	1	307.84	477	4.026
	2	307.99	599	4.040
	3	308.15	663	4.048
	6	308.73	736	4.110
N <sub>2</sub> (C-B) $\Delta v = -1$	0-1	357.7	$8.91 \times 10^6$	3.467
	1-2	353.6	$5.59 \times 10^6$	3.507
	2-3	350.0	$1.74 \times 10^6$	3.543
N <sub>2</sub> (C-B) $\Delta v = -2$	0-2	380.4	$3.55 \times 10^6$	3.259
	1-3	375.4	$4.93 \times 10^6$	3.301
	2-4	370.9	$4.06 \times 10^6$	3.342
N <sub>2</sub> (C-B) $\Delta v = -3$	0-3	405.8	$1.09 \times 10^6$	3.055
	1-4	399.7	$2.42 \times 10^6$	3.102
	2-5	394.2	$3.13 \times 10^6$	3.145

Table B.2 Boltzmann plot calculations for linear-field OH (A-X) spectra.

Power	Band Number	Relative Intensity	Y Axis	Slope	Temperature (K)
50 W	1	0.4426	-0.0490	-25.8129	449.58
	2	0.5736	-0.5279		
	3	0.7517	-0.6949		
	6	0.3232	-2.2606		
70 W	1	0.4094	-0.1270	-24.5898	471.94
	2	0.5481	-0.5733		
	3	0.6816	-0.7928		
	6	0.3304	-2.2386		
90 W	1	0.3898	-0.1761	-23.7414	488.81
	2	0.5197	-0.6265		
	3	0.6474	-0.8443		
	6	0.3351	-2.2244		

Table B.3 Boltzmann plot calculations for cross-field OH (A-X) spectra.

Power	Band Number	Relative Intensity	Y Axis	Slope	Temperature (K)
50 W	1	0.3871	-0.1830	-24.6618	470.56
	2	0.5502	-0.5695		
	3	0.7192	-0.7391		
	6	0.3216	-2.2656		
70 W	1	0.3626	-0.2485	-23.6636	490.41
	2	0.5288	-0.6093		
	3	0.6967	-0.7709		
	6	0.3292	-2.2421		
90 W	1	0.3540	-0.2724	-21.7838	532.73
	2	0.5137	-0.6382		
	3	0.6892	-0.7817		
	6	0.3713	-2.1219		

## APPENDIX C

### MATLAB Code – van der Waals Broadening

A set of MATLAB codes were developed to analyze ArI emission lines to determine the gas temperature of the plasma. This is an example file for the 696.5 ArI line.

```
1 % Program to calculate the gas temperature given a Voigt FWHM
2 % for the 696.5 ArI emission line.
3 % Created by Steven J. Doyle
4
5 %% INITIAL EQUATIONS & CONDITIONS
6
7 % L = STARK + VDW
8 % G = DOPPLER + INSTRUMENT
9 % G^2 = V^2 + V*L
10
11 % FOR FIRST CALCULATION OF GAS TEMPERATURE, ASSUME THE STARK
12 % COMPONENT IS % NEGLIGIBLE AND SOLVE THE EQUATIONS FOR THE
13 % TEMPERATURE.
14
15 %% VOIGT FWHM
16
17 V = [1.0618]; % FWHM of the 696.5 ArI emission line
18
19 %% DOPPLER
20
21 % DOPPLER = 7.16*10^-7 * LAMBDA * (T/M)^0.5
22
23 % DOPPLER GIVEN IN UNITS OF ANGSTROMS
24
25 % LAMBDA, EMISSION WAVELENGTH, ANGSTROM
26 % T, TEMPERATURE OF THE EMITTER OR GAS TEMPERATURE, KELVIN
27 % M, ATOMIC MASS, GRAM/MOLE
28
29 lambda_696 = 6965; % wavelength, Angstroms
30
31 M = 39.948; % atomic mass of argon, gram/mol
```

```

32
33 - doppler_696 = @(T) (7.16*10^-7*lambda_696)*((T/M)^0.5); % DOPPLER, Angstrom
34
35 %% INSTRUMENTAL
36
37 % NE-AR LASTER, OPERATING AT 632.8 NM WAVELENGTH
38
39 % READINGS RECORDED AT 300 DATA POINTS AND AVERAGED OVER 3 RUNS
40
41 - instrument_data = [0.99282 0.99319 0.99122];
42 - instrument = (instrument_data(1)+instrument_data(2)+...
43     instrument_data(3))/3; % INSTRUMENT, average, Angstrom
44
45 %% VDW
46
47 % VDW = 4.09*10^-13 * LAMBDA^2 * (ALPHA*R2)^(2/5) * (T/U)^(3/10) * N
48
49 % VDW GIVEN IN UNITS OF ANGSTROMS
50
51 % LAMBDA, EMISSION WAVELENGTH, ANGSTROMS
52 % T, TEMPERATURE OF THE EMITTER OR GAS TEMPERATURE, KELVIN
53 % ALPHA, AVERAGE POLARIZABILITY OF NEUTRAL PERTURBERS, CM^3
54 % N, PERTURBER DENSITY, CM^-3
55 % U, REDUCED MASS OF THE EMITTER-PERTURBER SYSTEM, GRAM/MOLE
56 % R2, MEAN SQUARE RADIUS OF THE EMITTING ATOM, CM^2
57
58 % AR-696.5 -- N = 4(P) TO N = 4(S)
59
60 %%%%%%%%%%%%%%%%%%%%%%%%%%%%%%%%%%%%%%%%%%%%%%%%%%%%%%%%%%%%%%%%%%%%%%%%%%% ALPHA %%%%%%%%%%%%%%%%%%%%%%%%%%%%%%%%%%%%%%%%%%%%%%%%%%%%%%%%%%%%%%%%%%%%%%%%%%%
61
62 - a0 = 5.29177*10^-9; % Bohr radius, cm

```

```

63 - alpha = 11.08*a0^3; % average polarizability of argon, cm^3
64
65 %%%%%%%%%%%%%%%%%%%%%%%%%%%%%%%%%%%%%%%%%%%%%%%%%%%%%%%%%%%%%%%%%%%%%%%%% N %%%%%%%%%%%%%%%%%%%%%%%%%%%%%%%%%%%%%%%%%%%%%%%%%%%%%%%%%%%%%%%%%%%%%%%%%
66
67 % p = nkT
68
69 % p = pressure, Pa
70 % n = atom density of neutral species (argon), cm^-3
71 % k = boltzmann's constant, J/K
72 % T = gas temperature, K
73
74 - p = 101325; % atmospheric pressure, Pa
75 - k = 1.38*10^-23; % boltzmann's constant, J/K
76
77 - n = @(T) (p/(k*T))/1000000; % atom density, cm^-3
78
79 %%%%%%%%%%%%%%%%%%%%%%%%%%%%%%%%%%%%%%%%%%%%%%%%%%%%%%%%%%%%%%%%%%%%%%%%% U %%%%%%%%%%%%%%%%%%%%%%%%%%%%%%%%%%%%%%%%%%%%%%%%%%%%%%%%%%%%%%%%%%%%%%%%%
80
81 % U = (M1*M2)/(M1+M2)
82
83 % U = REDUCED MASS OF THE EMITTER-PERTURBER SYSTEM, GRAM/MOLE (from kg)
84 % M1 = ATOMIC MASS OF ATOM 1, kg
85 % M2 = ATOMIC MASS OF ATOM 2, kg
86
87 - m_ar = 6.634*10^-26; % mass of 1 argon atom, kg
88
89 - u = (M*M)/(M+M); % reduced mass, gram/mol
90
91 %%%%%%%%%%%%%%%%%%%%%%%%%%%%%%%%%%%%%%%%%%%%%%%%%%%%%%%%%%%%%%%%%%%%%%%%% R2 %%%%%%%%%%%%%%%%%%%%%%%%%%%%%%%%%%%%%%%%%%%%%%%%%%%%%%%%%%%%%%%%%%%%%%%%%
92
93 - E_ion_h = 1312; % ionization energy of hydrogen, kJ/mole

```

```

94
95 - E_ion_emitter = 1520.6; % ionization energy of argon, kJ/mole
96
97 % AR-696.5 -- N = 4(P) TO N = 4(S)
98
99 - E_l_696 = 1114.25; % lower energy level, 4s orbital of Ar, kJ/mole
100 - E_u_696 = 1285.94; % upper energy level, 4p orbital of Ar, kJ/mole
101 - n_l_696 = E_ion_h/(E_ion_emitter-E_l_696); % lower effective quantum #
102 - n_u_696 = E_ion_h/(E_ion_emitter-E_u_696); % upper effective quantum #
103 - l_l_696 = 0; % lower angular quantum #, 4s orbital of Ar
104 - l_u_696 = 1; % upper angular quantum #, 4p orbital of Ar
105
106 - R2_l_696 = 0.5*n_l_696*((5*n_l_696)+1-((3*l_l_696)*(l_l_696+1))); % lower
107 - R2_u_696 = 0.5*n_u_696*((5*n_u_696)+1-((3*l_u_696)*(l_u_696+1))); % upper
108 - R2_696 = (R2_u_696-R2_l_696)*a0^2; % mean square radius of argon, cm^2
109
110 %%%%%%%%%%%%%%%%%%%%%%%%%%%%%%%%%%%%%%%%%%%%%%%%%%%%%%%%%%%%%%%%%%%%%%%%%
111
112 - vdw_696 = @(T) (4.09*10^-13)*(lambda_696^2)*((alpha*R2_696)^(2/5))*...
113 (T/u)^(3/10))*n; % VDW, Angstrom
114
115 %% GAS TEMPERATURE MEASUREMENT
116
117 - solve_696 = size(length(V));
118 - Tg_696 = size(length(V));
119
120 - for i = 1:length(V)
121
122 -     solve_696 = @(T) (instrument+((7.16*10^-7*lambda_696)...
123 *((T/M)^0.5)))^2 - V(i)^2 + (V(i)*(((4.09*10^-13)...
124 *(lambda_696^2)*(alpha*R2_696)^(2/5))*((T/u)^(3/10))...
125
126 -     *(p/(k*T))/1000000));
127 -     Tg_696(i) = fzero(solve_696,500);
128 - end
129
130 - display(Tg_696)

```

## APPENDIX D

### Data File Directory

All files can be found in the PERL directory folders in the Google Drive of the lab account.

Folder	
PERL/Data Directory/Steven/MatlabFiles	
File Name	Description
ARGON_696_5.m	Gas determination from VDW broadening for the 696.5 nm ArI emission line
ARGON_706_7.m	Gas determination from VDW broadening for the 706.7 nm ArI emission line
ARGON_738_3.m	Gas determination from VDW broadening for the 738.3 nm ArI emission line
ARGON_751_4.m	Gas determination from VDW broadening for the 751.4 nm ArI emission line
ARGON_763_5.m	Gas determination from VDW broadening for the 763.5 nm ArI emission line
ARGON_794_8.m	Gas determination from VDW broadening for the 794.8 nm ArI emission line
ARGON_800_6.m	Gas determination from VDW broadening for the 800.6 nm ArI emission line
ARGON_801_4.m	Gas determination from VDW broadening for the 801.4 nm ArI emission line
ARGON_810_4.m	Gas determination from VDW broadening for the 810.4 nm ArI emission line
ARGON_811_5.m	Gas determination from VDW broadening for the 811.5 nm ArI emission line
ARGON_826_4.m	Gas determination from VDW broadening for the 826.4 nm ArI emission line
ARGON_840_8.m	Gas determination from VDW broadening for the 840.8 nm ArI emission line
ARGON_842_4.m	Gas determination from VDW broadening for the 842.4 nm ArI emission line
ARGON_852_1.m	Gas determination from VDW broadening for the 851.1 nm ArI emission line

Folder	
PERL/Data Directory/Steven/Data Sheets & Manuals	
Folder	Description
Equipment Datasheets & Manuals	Contains Datasheets and User Manuals for the function generator, power supply, and pulse generator
Experimental Procedures and Manuals	Contains Standard Operating Procedures and User Manuals for techniques

Folder	
PERL/Data Directory/Steven/Data	
Folder	Description
Scanning Electron Microscopy Results	Contains SEM images from UA and UAH SEM facilities
Surface Properties – Plasma Treatment	Contains RAMAN and contact angle results for 2016 summer research project with Dr. Waddell
Langmuir Probes	Contains results for Langmuir probe experiments
Optical Emission Spectroscopy	Contains OES data from experiments

## REFERENCES

- [1] M. Laroussi and X. Lu, "Room-temperature atmospheric pressure plasma plume for biomedical applications," *Appl. Phys. Lett.*, vol. 87, no. 11, pp. 1–3, 2005.
- [2] S. Bornholdt, M. Wolter, and H. Kersten, "Characterization of an atmospheric pressure plasma jet for surface modification and thin film deposition," *Eur. Phys. J. D*, vol. 60, no. 3, pp. 653–660, 2010.
- [3] M. Keidar, "Factors affecting synthesis of single wall carbon nanotubes in arc discharge," *J. Phys. D. Appl. Phys.*, vol. 40, no. 8, pp. 2388–2393, Apr. 2007.
- [4] T. Nozaki, K. Ohnishi, K. Okazaki, and U. Kortshagen, "Fabrication of vertically aligned single-walled carbon nanotubes in atmospheric pressure non-thermal plasma CVD," *Carbon N. Y.*, vol. 45, no. 2, pp. 364–374, 2007.
- [5] T. Nozaki and K. Okazaki, "Carbon nanotube synthesis in atmospheric pressure glow discharge: A review," *Plasma Processes and Polymers*, vol. 5, no. 4. WILEY-VCH Verlag, pp. 300–321, 13-Jun-2008.
- [6] O. Smiljanic, B. L. Stansfield, J.-P. Dodelet, A. Serventi, and S. Désilets, "Gas-phase synthesis of SWNT by an atmospheric pressure plasma jet," 2002.
- [7] S.-J. Kyung, Y.-H. Lee, C. Kim, J.-H. Lee, and G.-Y. Yeom, "Field emission properties of carbon nanotubes synthesized by capillary type atmospheric pressure plasma enhanced chemical vapor deposition at low temperature," *Carbon N. Y.*, vol. 44, no. 8, pp. 1530–1534, 2006.
- [8] Y. Zhang, H. Gu, and S. Iijima, "Single-wall carbon nanotubes synthesized by laser ablation in a nitrogen atmosphere," *Appl. Phys. Lett.*, vol. 73, no. 26, p. 3827, 1998.
- [9] O. Jašek, M. Eliáš, L. Zajíčková, V. Kudrle, M. Bublan, J. Matějková, A. Rek, J. Buršík, and M. Kadlečíková, "Carbon nanotubes synthesis in microwave plasma torch at atmospheric pressure," *Mater. Sci. Eng. C*, vol. 26, no. 5, pp. 1189–1193, 2006.
- [10] K. Yoshie, S. Kasuya, K. Eguchi, and T. Yoshida, "Novel method for C<sub>60</sub> synthesis: A thermal plasma at atmospheric pressure," *Appl. Phys. Lett.*, vol. 61, no. 23, pp. 2782–2783, Dec. 1992.
- [11] O. Matsumoto, T. Kotaki, H. Shikano, K. Takemura, and S. Tanaka, "Synthesis of Carbon Nitride in Plasma Arc," *J. Electrochem. Soc.*, vol. 141, no. 2, p. L16, 1994.
- [12] Y. Sawada, S. Ogawa, and M. Kogoma, "Synthesis of plasma-polymerized tetraethoxysilane and hexamethyldisiloxane films prepared by atmospheric pressure glow discharge," *J. Phys. D. Appl. Phys.*, vol. 28, no. 8, pp. 1661–1669, Aug. 1995.

- [13] S. E. Babayan, J. Y. Jeong, V. J. Tu, J. Park, G. S. Selwyn, and R. F. Hicks, "Deposition of silicon dioxide films with an atmospheric-pressure plasma jet," *Plasma Sources Sci. Technol.*, vol. 7, no. 3, pp. 286–288, Aug. 1998.
- [14] J. Benedikt, V. Raballand, A. Yanguas-Gil, K. Focke, and A. von Keudell, "Thin film deposition by means of atmospheric pressure microplasma jet," *Plasma Phys. Control. Fusion*, vol. 49, no. 12B, pp. B419–B427, 2007.
- [15] N. Ohtake and M. Yoshikawa, "Diamond Film Preparation by Arc Discharge Plasma Jet Chemical Vapor Deposition in the Methane Atmosphere," *J. Electrochem. Soc.*, vol. 137, no. 2, p. 717, 1990.
- [16] W. Han, P. Redlich, F. Ernst, and M. Rühle, "Synthesis of GaN–carbon composite nanotubes and GaN nanorods by arc discharge in nitrogen atmosphere," *Appl. Phys. Lett.*, vol. 76, no. 5, pp. 652–654, 2000.
- [17] W. Han, P. Kohler-Redlich, F. Ernst, and M. Rühle, "Growth and microstructure of Ga<sub>2</sub>O<sub>3</sub> nanorods," *Solid State Commun.*, vol. 115, no. 10, pp. 527–529, 2000.
- [18] Y. C. Hong, J. H. Kim, C. U. Bang, and H. S. Uhm, "Gas-phase synthesis of nitrogen-doped TiO<sub>2</sub> nanorods by microwave plasma torch at atmospheric pressure," *Phys. Plasmas*, vol. 12, no. 11, p. 114501, Nov. 2005.
- [19] W.-H. Chiang, C. Richmonds, and R. M. Sankaran, "Continuous-flow, atmospheric-pressure microplasmas: a versatile source for metal nanoparticle synthesis in the gas or liquid phase," *Plasma Sources Sci. Technol.*, vol. 19, no. 3, p. 034011, Jun. 2010.
- [20] C. Richmonds and R. M. Sankaran, "Plasma-liquid electrochemistry: Rapid synthesis of colloidal metal nanoparticles by microplasma reduction of aqueous cations," *Appl. Phys. Lett.*, vol. 93, no. 13, p. 131501, Sep. 2008.
- [21] H.-F. Lin, S.-C. Liao, and S.-W. Hung, "The dc thermal plasma synthesis of ZnO nanoparticles for visible-light photocatalyst," *J. Photochem. Photobiol. A Chem.*, vol. 174, no. 1, pp. 82–87, 2005.
- [22] T. Ghodselahi, M. A. Vesaghi, A. Gelali, H. Zahrabi, and S. Solaymani, "Morphology, optical and electrical properties of Cu–Ni nanoparticles in a-C:H prepared by co-deposition of RF-sputtering and RF-PECVD," *Appl. Surf. Sci.*, vol. 258, no. 2, pp. 727–731, 2011.
- [23] V. Vons, Y. Creighton, and A. Schmidt-Ott, "Nanoparticle production using atmospheric pressure cold plasma," *J. Nanoparticle Res.*, vol. 8, no. 5, pp. 721–728, Nov. 2006.
- [24] Y. Shimizu, T. Sasaki, T. Ito, K. Terashima, and N. Koshizaki, "Fabrication of spherical carbon via UHF inductively coupled microplasma CVD," *J. Phys. D: Appl. Phys.*, vol. 36, no. 23, pp. 2940–2944, 2003.
- [25] Y. Shimizu, T. Sasaki, A. Chandra Bose, K. Terashima, and N. Koshizaki,

- “Development of wire spraying for direct micro-patterning via an atmospheric-pressure UHF inductively coupled microplasma jet,” *Surf. Coatings Technol.*, vol. 200, no. 14–15, pp. 4251–4256, 2006.
- [26] S. Horikoshi and N. Serpone, “Introduction to Nanoparticles,” in *Microwaves in Nanoparticle Synthesis: Fundamentals and Applications*, Wiley-VCH, 2013, pp. 1–24.
- [27] D. Mariotti and R. M. Sankaran, “Perspectives on atmospheric-pressure plasmas for nanofabrication,” *J. Phys. D. Appl. Phys.*, vol. 44, no. 17, p. 174023, 2011.
- [28] R. Mohan Sankaran, Dean Holunga, and Richard C. Flagan, and K. P. Giapis\*, “Synthesis of Blue Luminescent Si Nanoparticles Using Atmospheric-Pressure Microdischarges,” 2005.
- [29] C.-H. Kim, J. H. Bahn, S.-H. Lee, G.-Y. Kim, S.-I. Jun, K. Lee, and S. J. Baek, “Induction of cell growth arrest by atmospheric non-thermal plasma in colorectal cancer cells,” *J. Biotechnol.*, vol. 150, no. 4, pp. 530–538, 2010.
- [30] M. Keidar, R. Walk, A. Shashurin, P. Srinivasan, A. Sandler, S. Dasgupta, R. Ravi, R. Guerrero-Preston, and B. Trink, “Cold plasma selectivity and the possibility of a paradigm shift in cancer therapy,” *Br. J. Cancer*, vol. 105, no. 9, pp. 1295–1301, Oct. 2011.
- [31] G. C. Kim, G. J. Kim, S. R. Park, S. M. Jeon, H. J. Seo, F. Iza, and J. K. Lee, “Air plasma coupled with antibody-conjugated nanoparticles: a new weapon against cancer,” *J. Phys. D. Appl. Phys.*, vol. 42, no. 3, p. 032005, Feb. 2009.
- [32] N. Georgescu and A. R. Lupu, “Tumoral and Normal Cells Treatment With High-Voltage Pulsed Cold Atmospheric Plasma Jets,” *IEEE Trans. Plasma Sci.*, vol. 38, no. 8, pp. 1949–1955, Aug. 2010.
- [33] D. B. Graves, “Reactive Species from Cold Atmospheric Plasma: Implications for Cancer Therapy,” *Plasma Process. Polym.*, vol. 11, no. 12, pp. 1120–1127, Dec. 2014.
- [34] M. Keidar, A. Shashurin, O. Volotskova, M. Ann Stepp, P. Srinivasan, A. Sandler, and B. Trink, “Cold atmospheric plasma in cancer therapy,” *Phys. Plasmas*, vol. 20, no. 5, p. 057101, May 2013.
- [35] Xinpei Lu, Yinguang Cao, Ping Yang, Qing Xiong, Zilan Xiong, Yubin Xian, and Yuan Pan, “An SRC\$ Plasma Device for Sterilization of Root Canal of Teeth,” *IEEE Trans. Plasma Sci.*, vol. 37, no. 5, pp. 668–673, May 2009.
- [36] Q. S. Yu, C. Huang, F.-H. Hsieh, H. Huff, and Y. Duan, “Bacterial inactivation using a low-temperature atmospheric plasma brush sustained with argon gas,” *J. Biomed. Mater. Res. Part B Appl. Biomater.*, vol. 80B, no. 1, pp. 211–219, Jan. 2007.
- [37] S. Rupf, A. Lehmann, M. Hannig, B. Schafer, A. Schubert, U. Feldmann, and A.

- Schindler, "Killing of adherent oral microbes by a non-thermal atmospheric plasma jet," *J. Med. Microbiol.*, vol. 59, no. 2, pp. 206–212, Feb. 2010.
- [38] G. Fridman, A. D. Brooks, M. Balasubramanian, A. Fridman, A. Gutsol, V. N. Vasilets, H. Ayan, and G. Friedman, "Comparison of Direct and Indirect Effects of Non-Thermal Atmospheric-Pressure Plasma on Bacteria," *Plasma Process. Polym.*, vol. 4, no. 4, pp. 370–375, May 2007.
- [39] J. Choi, A.-A. H. Mohamed, S. K. Kang, K. C. Woo, K. T. Kim, and J. K. Lee, "900-MHz Nonthermal Atmospheric Pressure Plasma Jet for Biomedical Applications," *Plasma Process. Polym.*, vol. 7, no. 3–4, pp. 258–263, Mar. 2010.
- [40] Q. S. Yu, C. Huang, F.-H. Hsieh, H. Huff, and Y. Duan, "Sterilization effects of atmospheric cold plasma brush," *Appl. Phys. Lett.*, vol. 88, no. 1, p. 013903, Jan. 2006.
- [41] X. Lu, Z. Xiong, F. Zhao, Y. Xian, Q. Xiong, W. Gong, C. Zou, Z. Jiang, and Y. Pan, "A simple atmospheric pressure room-temperature air plasma needle device for biomedical applications," *Appl. Phys. Lett.*, vol. 95, no. 18, p. 181501, Nov. 2009.
- [42] E. Stoffels, Y. Sakiyama, and D. B. Graves, "Cold Atmospheric Plasma: Charged Species and Their Interactions With Cells and Tissues," *IEEE Trans. Plasma Sci.*, vol. 36, no. 4, pp. 1441–1457, Aug. 2008.
- [43] G. Y. Park, S. J. Park, M. Y. Choi, I. G. Koo, J. H. Byun, J. W. Hong, J. Y. Sim, G. J. Collins, and J. K. Lee, "Atmospheric-pressure plasma sources for biomedical applications," *Plasma Sources Sci. Technol.*, vol. 21, no. 4, p. 043001, Aug. 2012.
- [44] X. Lu, Z. Jiang, Q. Xiong, Z. Tang, and Y. Pan, "A single electrode room-temperature plasma jet device for biomedical applications," *Appl. Phys. Lett.*, vol. 92, no. 15, pp. 15–17, 2008.
- [45] P. B. and R. Brandenburg, "Atmospheric pressure discharge filaments and microplasmas: physics, chemistry and diagnostics," *J. Phys. D. Appl. Phys.*, vol. 46, no. 46, p. 464001, 2013.
- [46] M. Moselhy, I. Petzenhauser, K. Frank, and K. H. Schoenbach, "Excimer emission from microhollow cathode argon discharges," *J. Phys. D. Appl. Phys.*, vol. 36, no. 23, pp. 2922–2927, Dec. 2003.
- [47] D. Mariotti, "Nonequilibrium and effect of gas mixtures in an atmospheric microplasma," *Appl. Phys. Lett.*, vol. 92, no. 15, p. 151505, Apr. 2008.
- [48] X.-M. Zhu, W.-C. Chen, and Y.-K. Pu, "Gas temperature, electron density and electron temperature measurement in a microwave excited microplasma," *J. Phys. D. Appl. Phys.*, vol. 41, no. 10, p. 105212, May 2008.
- [49] F. Iza, J. K. Lee, and M. G. Kong, "Electron Kinetics in Radio-Frequency Atmospheric-Pressure Microplasmas," *Phys. Rev. Lett.*, vol. 99, no. 7, p. 075004,

Aug. 2007.

- [50] J. Choi, F. Iza, J. K. Lee, and C.-M. Ryu, "Electron and Ion Kinetics in a DC Microplasma at Atmospheric Pressure," *IEEE Trans. Plasma Sci.*, vol. 35, no. 5, pp. 1274–1278, Oct. 2007.
- [51] K. G. Xu and S. J. Doyle, "Measurement of atmospheric pressure microplasma jet with Langmuir probes Measurement of atmospheric pressure microplasma jet with Langmuir probes," *J. Vac. Sci. Technol. A*, vol. 34, no. 5, 2016.
- [52] X. M. Zhu, Y. K. Pu, N. Balcon, R. Boswell, and L. M. A, "Measurement of the electron density in atmospheric-pressure low-temperature argon discharges by line-ratio method of optical emission spectroscopy," *J. Phys. D. Appl. Phys.*, vol. 42, no. 14, p. 142003, Jul. 2009.
- [53] D. Mariotti, Y. Shimizu, T. Sasaki, and N. Koshizaki, "Gas temperature and electron temperature measurements by emission spectroscopy for an atmospheric microplasma," *J. Appl. Phys.*, vol. 101, no. 1, p. 013307, Jan. 2007.
- [54] A. Yanguas-Gil, J. Cotrino, and A. R. González-Elipe, "Measuring the electron temperature by optical emission spectroscopy in two temperature plasmas at atmospheric pressure: A critical approach," *J. Appl. Phys.*, vol. 99, no. 3, p. 033104, Feb. 2006.
- [55] J. J. Narendra, T. A. Grotjohn, and J. Asmussen, "Microstripline applicators for creating microplasma discharges with microwave energy," *Plasma Sources Sci. Technol.*, vol. 17, no. 3, p. 035027, Aug. 2008.
- [56] S. Hofmann, a F. H. van Gessel, T. Verreycken, and P. Bruggeman, "Power dissipation, gas temperatures and electron densities of cold atmospheric pressure helium and argon RF plasma jets," *Plasma Sources Sci. Technol.*, vol. 20, no. 6, p. 065010, 2011.
- [57] Q. Y. Zhang, D. Q. Shi, W. Xu, C. Y. Miao, C. Y. Ma, C. S. Ren, C. Zhang, and Z. Yi, "Determination of vibrational and rotational temperatures in highly constricted nitrogen plasmas by fitting the second positive system of  $N_2$  molecules," *AIP Adv.*, vol. 5, no. 5, 2015.
- [58] C.-J. Chen and S.-Z. Li, "Spectroscopic measurement of plasma gas temperature of the atmospheric-pressure microwave induced nitrogen plasma torch," *Plasma Sources Sci. Technol.*, vol. 24, no. 3, p. 035017, 2015.
- [59] X.-M. Zhu and Y.-K. Pu, "Optical emission spectroscopy in low-temperature plasmas containing argon and nitrogen: determination of the electron temperature and density by the line-ratio method," *J. Phys. D. Appl. Phys.*, vol. 43, no. 40, p. 403001, 2010.
- [60] K. Niemi, S. Reuter, L. Schaper, N. Knake, V. S. Der Gathen, and T. Gans, "Diagnostics on an atmospheric pressure plasma jet," *J. Phys. Conf. Ser.*, vol. 71,

p. 012012, 2007.

- [61] J.-Y. Choi, N. Takano, K. Urabe, and K. Tachibana, "Measurement of electron density in atmospheric pressure small-scale plasmas using CO<sub>2</sub>-laser heterodyne interferometry," *Plasma Sources Sci. Technol.*, vol. 18, p. 035013, 2009.
- [62] H. Rabat and C. De Izarra, "Check of OH rotational temperature using an interferometric method," *J. Phys. D. Appl. Phys.*, vol. 37, no. 17, pp. 2371–2375, 2004.
- [63] A. F. H. van Gessel, E. A. D. Carbone, P. J. Bruggeman, and J. J. A. M. van der Mullen, "Laser scattering on an atmospheric pressure plasma jet: disentangling Rayleigh, Raman and Thomson scattering," *Plasma Sources Sci. Technol.*, vol. 21, no. 1, p. 15003, 2012.
- [64] M. Christova, E. Castanos-Martinez, M. D. Calzada, Y. Kabouzi, J. M. Luque, and M. Moisan, "Electron density and gas temperature from line broadening in an argon surface-wave-sustained discharge at atmospheric pressure," *Appl. Spectrosc.*, vol. 58, no. 9, pp. 1032–1037, 2004.
- [65] M. R. Talukder, D. Korzec, and M. Kando, "Probe diagnostics of high pressure microwave discharge in helium," *J. Appl. Phys.*, vol. 91, no. 12, p. 9529, 2002.
- [66] H. E. Porteanu, S. Kühn, and R. Gesche, "Electric probe investigations of microwave generated, atmospheric pressure, plasma jets," *J. Appl. Phys.*, vol. 108, no. 1, p. 013301, Jul. 2010.
- [67] L. Prevosto, H. Kelly, and B. R. Mancinelli, "Langmuir probe diagnostics of an atmospheric pressure, vortex-stabilized nitrogen plasma jet," *J. Appl. Phys.*, vol. 112, no. 6, p. 063302, Sep. 2012.
- [68] S. Saito, M. A. Razzak, S. Takamura, and M. R. Talukder, "Development of asymmetric double probe formula and its application for collisional plasmas," *J. Appl. Phys.*, vol. 107, no. 12, p. 123306, Jun. 2010.
- [69] A. Shashurin, J. Li, T. Zhuang, M. Keidar, and I. I. Beilis, "Application of electrostatic Langmuir probe to atmospheric arc plasmas producing nanostructures," *Phys. Plasmas*, vol. 18, no. 7, p. 073505, Jul. 2011.
- [70] A. Ionascut-Nedelcescu, C. Carlone, U. Kogelschatz, D. V. Gravelle, and M. I. Boulos, "Calculation of the gas temperature in a throughflow atmospheric pressure dielectric barrier discharge torch by spectral line shape analysis," *J. Appl. Phys.*, vol. 103, no. 6, 2008.
- [71] X. Lu, M. Laroussi, and V. Puech, "On atmospheric-pressure non-equilibrium plasma jets and plasma bullets," *Plasma Sources Sci. Technol.*, vol. 21, no. 3, p. 034005, 2012.
- [72] A. C. Bose, Y. Shimizu, D. Mariotti, T. Sasaki, K. Terashima, and N. Koshizaki, "Flow rate effect on the structure and morphology of molybdenum oxide

- nanoparticles deposited by atmospheric-pressure microplasma processing,” *Nanotechnology*, vol. 17, no. 24, pp. 5976–5982, Dec. 2006.
- [73] D. Mariotti, A. C. Bose, and K. Ostrikov, “Atmospheric-Microplasma-Assisted Nanofabrication: Metal and Metal–Oxide Nanostructures and Nanoarchitectures,” *IEEE Trans. Plasma Sci.*, vol. 37, no. 6, pp. 1027–1033, Jun. 2009.
- [74] H. S. Park, S. J. Kim, H. M. Joh, T. H. Chung, S. H. Bae, and S. H. Leem, “Optical and electrical characterization of an atmospheric pressure microplasma jet with a capillary electrode,” *Phys. Plasmas*, vol. 17, no. 3, 2010.
- [75] J. Torres, J. Jonkers, M. J. Van De Sande, J. J. a M. Van Der Mullen, a Gamero, and a Sola, “An easy way to determine simultaneously the electron density and temperature in high-pressure plasmas by using Stark broadening,” *J. Phys. D. Appl. Phys.*, vol. 36, no. 13, pp. L55–L59, 2003.
- [76] A. F. H. van Gessel, E. A. D. Carbone, P. J. Bruggeman, and Van der Mullen J J A M, “Laser scattering on an atmospheric pressure plasma jet: disentangling Rayleigh, Raman and Thomson scattering,” *Plasma Sources Sci. Technol.*, vol. 21, no. 1, p. 015003, Feb. 2012.
- [77] F. Iza and J. a. Hopwood, “Rotational, vibrational, and excitation temperatures of a microwave-frequency microplasma,” *IEEE Trans. Plasma Sci.*, vol. 32, no. 2, pp. 498–504, 2004.
- [78] M. D. Calzada, “Spectroscopy of the discharges created and maintained by a surface-wave,” *Mem. della Soc. Astron. Ital. Suppl. v.7, p.198*, vol. 7, p. 198, 2005.
- [79] M. D. Calzada, “Spectroscopy methods applied to the research in plasmas at atmospheric pressure,” vol. 133, 2008.
- [80] C. Wang, N. Srivastava, S. Scherrer, P.-R. Jang, T. S. Dibble, and Y. Duan, “Optical diagnostics of a low power—low gas flow rates atmospheric-pressure argon plasma created by a microwave plasma torch,” *Plasma Sources Sci. Technol.*, vol. 18, no. 2, p. 025030, May 2009.
- [81] A. Sarani, A. Y. Nikiforov, and C. Leys, “Atmospheric pressure plasma jet in Ar and Ar/H<sub>2</sub>O mixtures: Optical emission spectroscopy and temperature measurements,” *Phys. Plasmas*, vol. 17, no. 6, p. 8pp, 2010.
- [82] S. Pellerin, K. Musiol, B. Pokrzywka, and J. Chapelle, “Stark width of Ar I transition (696.543 nm),” *J. Phys. B At. Mol. Opt. Phys.*, vol. 29, no. 17, p. 3911, 1996.
- [83] A. Kramida, Y. Ralchenko, J. Reader, and N. A. Team, “Nist Atomic Spectra Database (ver. 5.3),” 2015. [Online]. Available: [http://physics.nist.gov/PhysRefData/ASD/lines\\_form.html](http://physics.nist.gov/PhysRefData/ASD/lines_form.html). [Accessed: 21-Jul-2016].
- [84] G. Norlén, “Wavelengths and Energy Levels of Ar I and Ar II based on New

- Interferometric Measurements in the Region 3 400-9 800 Å,” *Phys. Scr.*, vol. 8, no. 6, pp. 249–268, Dec. 1973.
- [85] X.-M. Zhu and Y.-K. Pu, “A simple collisional–radiative model for low-temperature argon discharges with pressure ranging from 1 Pa to atmospheric pressure: kinetics of Paschen 1s and 2p levels,” *J. Phys. D. Appl. Phys.*, vol. 43, no. 1, p. 015204, Jan. 2010.
- [86] N. Konjević, “Plasma broadening and shifting of non-hydrogenic spectral lines: present status and applications,” *Phys. Rep.*, vol. 316, no. 6, pp. 339–401, 1999.
- [87] H.-J. Kunze, *Introduction to plasma spectroscopy*. Springer, 2009.
- [88] J. L. Walsh and M. G. Kong, “Contrasting characteristics of linear-field and cross-field atmospheric plasma jets,” *Appl. Phys. Lett.*, vol. 93, no. 11, 2008.
- [89] S. Djurović and N. Konjević, “On the use of non-hydrogenic spectral lines for low electron density and high pressure plasma diagnostics,” *Plasma Sources Sci. Technol.*, vol. 18, no. 3, p. 035011, Aug. 2009.
- [90] A. Ionascut-Nedelcescu, C. Carlone, U. Kogelschatz, C. Nessim, D. V. Gravelle, and M. I. Boulos, “Paper No. 00081,” in *Proceedings of the 18th International Symposium on Plasma Chemistry*, 2007.
- [91] P. B. and F. I. and P. G. and D. L. and M. G. K. and Y. A. G. and C. L. and D. C. Schram, “Electronic quenching of OH(A) by water in atmospheric pressure plasmas and its influence on the gas temperature determination by OH(A – X) emission,” *Plasma Sources Sci. Technol.*, vol. 19, no. 1, p. 15016, 2010.
- [92] T. Verreycken, a F. H. van Gessel, a Pageau, and P. Bruggeman, “Validation of gas temperature measurements by OES in an atmospheric air glow discharge with water electrode using Rayleigh scattering,” *Plasma Sources Sci. Technol.*, vol. 20, no. 2, p. 024002, 2011.
- [93] D. L. Rusterholtz, D. A. Lacoste, G. D. Stancu, D. Z. Pai, and C. O. Laux, “Ultrafast heating and oxygen dissociation in atmospheric pressure air by nanosecond repetitively pulsed discharges,” *J. Phys. D. Appl. Phys.*, vol. 46, no. 46, p. 464010, Nov. 2013.
- [94] C. O. Laux, T. G. Spence, C. H. Kruger, and R. N. Zare, “Optical diagnostics of atmospheric pressure air plasmas,” *Plasma Sources Sci. Technol.*, vol. 12, no. 2, pp. 125–138, May 2003.
- [95] N. Britun, M. Gaillard, A. Ricard, Y. M. Kim, K. S. Kim, and J. G. Han, “Determination of the vibrational, rotational and electron temperatures in N<sub>2</sub> and Ar–N<sub>2</sub> rf discharge,” *J. Phys. D. Appl. Phys.*, vol. 40, no. 4, pp. 1022–1029, 2007.
- [96] J. Luque and D. R. Crosley, “SRI International Report MP,” 1999.
- [97] P. Bruggeman, T. Verreycken, M. Á. González, J. L. Walsh, M. G. Kong, C. Leys,

- and D. C. Schram, "Optical emission spectroscopy as a diagnostic for plasmas in liquids: opportunities and pitfalls," *J. Phys. D. Appl. Phys.*, vol. 43, no. 12, p. 124005, Mar. 2010.
- [98] N. A. Popov, "Kinetic processes initiated by a nanosecond high-current discharge in hot air," *Plasma Phys. Reports*, vol. 37, no. 9, p. 807, 2011.
- [99] M. Mavadat, A. Ricard, C. Sarra-Bournet, and G. Laroche, "Determination of ro-vibrational excitations of  $N_2(B, v')$  and  $N_2(C, v')$  states in  $N_2$  microwave discharges using visible and IR spectroscopy," *J. Phys. D. Appl. Phys.*, vol. 44, no. 15, p. 155207, Apr. 2011.
- [100] C. D. Scott, H. E. Blackwell, S. Arepalli, and M. A. Akundi, "Techniques for Estimating Rotational and Vibrational Temperature in Nitrogen Arcjet Flow," *J. Thermophys. Heat Transf.*, vol. 12, no. 4, pp. 457–464, Oct. 1998.
- [101] S.-Z. Li, C.-J. Chen, X. Zhang, J. Zhang, and Y.-X. Wang, "Spectroscopic diagnosis of an atmospheric-pressure waveguide-based microwave  $N_2$ -Ar plasma torch," *Plasma Sources Sci. Technol.*, vol. 24, no. 2, p. 025003, Apr. 2015.
- [102] C. O. Laux, R. J. Gessman, C. H. Kruger, F. Roux, F. Michaud, and S. P. Davis, "Rotational temperature measurements in air and nitrogen plasmas using the first negative system of  $N_2^+$ ," *J. Quant. Spectrosc. Radiat. Transf.*, vol. 68, no. 4, pp. 473–482, 2001.
- [103] P. Bruggeman, D. C. Schram, M. G. Kong, and C. Leys, "Is the Rotational Temperature of OH(A-X) for Discharges in and in Contact with Liquids a Good Diagnostic for Determining the Gas Temperature?," *Plasma Process. Polym.*, vol. 6, no. 11, pp. 751–762, Nov. 2009.
- [104] J. Torres, J. M. Palomares, A. Sola, J. J. A. M. van der Mullen, and A. Gamero, "A Stark broadening method to determine simultaneously the electron temperature and density in high-pressure microwave plasmas," *J. Phys. D. Appl. Phys.*, vol. 40, no. 19, pp. 5929–5936, Oct. 2007.
- [105] J. Torres, M. J. Van De Sande, J. J. A. M. Van Der Mullen, A. Gamero, and A. Sola, "Stark broadening for simultaneous diagnostics of the electron density and temperature in atmospheric microwave discharges," 2006.
- [106] H. R. Griem, A. C. Kolb, and K. Y. Shen, "Stark Profile Calculations for the H $\beta$  Line of Hydrogen," *Astrophys. J.*, vol. 135, p. 272, 1962.
- [107] P. Kepple and H. R. Griem, "Improved Stark Profile Calculations for the Hydrogen Lines H $\alpha$ , H $\beta$ , H $\gamma$ , and H $\delta$ ," *Phys. Rev.*, vol. 173, no. 1, pp. 317–325, Sep. 1968.
- [108] M. A. Gigosos, M. Á. González, and V. Cardeñoso, "Computer simulated Balmer-alpha, -beta and -gamma Stark line profiles for non-equilibrium plasmas diagnostics," *Spectrochim. Acta Part B At. Spectrosc.*, vol. 58, no. 8, pp. 1489–

1504, 2003.

- [109] M. A. Gigosos and V. Cardeñoso, “New plasma diagnosis tables of hydrogen Stark broadening including ion dynamics,” *J. Phys. B At. Mol. Opt. Phys.*, vol. 29, no. 20, pp. 4795–4838, Oct. 1996.
- [110] M. . García, A. Rodero, A. Sola, and A. Gamero, “Experimental study of the creation of a surface-wave-sustained argon plasma column at atmospheric pressure,” *Spectrochim. Acta Part B At. Spectrosc.*, vol. 57, no. 11, pp. 1727–1737, 2002.
- [111] M. . García, A. Rodero, A. Sola, and A. Gamero, “Spectroscopic study of a stationary surface-wave sustained argon plasma column at atmospheric pressure,” *Spectrochim. Acta Part B At. Spectrosc.*, vol. 55, no. 11, pp. 1733–1745, 2000.
- [112] M. D. Calzada, A. Rodero, A. Sola, and A. Gamero, “Excitation Kinetic in an Argon Plasma Column Produced by a Surface Wave at Atmospheric Pressure,” *J. Phys. Soc. Japan*, vol. 65, no. 4, pp. 948–954, Apr. 1996.
- [113] H. R. Griem, *Principles of Plasma Spectroscopy*. Cambridge Univ. Press, 2005.
- [114] T. Wujec, H. W. Janus, and W. Jele ski, “Spectroscopic measurements of electric field distributions in dielectric barrier discharges in hydrogen,” *J. Phys. D. Appl. Phys.*, vol. 36, no. 7, pp. 868–877, Apr. 2003.
- [115] C. H. Su and S. H. Lam, “Continuum Theory of Spherical Electrostatic Probes,” *Phys. Fluids*, vol. 6, no. 10, p. 1479, 1963.
- [116] P. R. Smy, “The use of Langmuir probes in the study of high pressure plasmas,” *Adv. Phys.*, vol. 25, no. 5, pp. 517–553, Sep. 1976.
- [117] R. M. Clements, “Plasma diagnostics with electric probes,” *J. Vac. Sci. Technol.*, vol. 15, no. 2, pp. 193–198, Mar. 1978.
- [118] R. E. Kiel, “Continuum Electrostatic Probe Theory for Large Sheaths on Spheres and Cylinders,” *J. Appl. Phys.*, vol. 40, no. 9, pp. 3668–3673, Aug. 1969.
- [119] C. S. MacLatchy, “Langmuir probe measurements of ion density in an atmospheric-pressure air-propane flame,” *Combust. Flame*, vol. 36, pp. 171–178, Jan. 1979.
- [120] C. S. MacLatchy and H. C. L. Smith, “The electron current to a Langmuir probe in a flowing high-pressure plasma,” *IEEE Trans. Plasma Sci.*, vol. 19, no. 6, pp. 1254–1258, 1991.
- [121] H. R. Griem, *Plasma Spectroscopy*. New York: McGraw-Hill, 1964.
- [122] P. S. Moussounda and P. Ranson, “Pressure broadening of argon lines emitted by a high-pressure microwave discharge (Surfatron),” *J. Phys. B At. Mol. Phys.*, vol. 20, no. 5, pp. 949–961, Mar. 1987.

- [123] H. R. Griem, *Spectral line broadening by plasmas*. Academic Press, 1974.
- [124] J. M. Luque, M. D. Calzada, and M. Saez, "Experimental research into the influence of ion dynamics when measuring the electron density from the Stark broadening of the H and H lines," *J. Phys. B At. Mol. Opt. Phys.*, vol. 36, no. 8, pp. 1573–1584, Apr. 2003.
- [125] I. L. Chidsey and D. R. Crosley, "Calculated rotational transition probabilities for the A–X system of OH," *J. Quant. Spectrosc. Radiat. Transf.*, vol. 23, no. 2, pp. 187–199, Feb. 1980.
- [126] G. H. Dieke and H. M. Crosswhite, "The ultraviolet bands of OH Fundamental data," *J. Quant. Spectrosc. Radiat. Transf.*, vol. 2, no. 2, pp. 97–199, Apr. 1962.
- [127] C. O. Laux and C. H. Kruger, "Arrays of radiative transition probabilities for the N<sub>2</sub> first and second positive, no beta and gamma, N<sub>2</sub><sup>+</sup> first negative, and O<sub>2</sub> Schumann-Runge band systems," *J. Quant. Spectrosc. Radiat. Transf.*, vol. 48, no. 1, pp. 9–24, 1992.
- [128] F. R. Gilmore, R. R. Laher, and P. J. Espy, "Franck–Condon Factors, r-Centroids, Electronic Transition Moments, and Einstein Coefficients for Many Nitrogen and Oxygen Band Systems," *J. Phys. Chem. Ref. Data*, vol. 21, no. 5, pp. 1005–1107, 1992.
- [129] P. R. Smy, "The use of Langmuir probes in the study of high pressure plasmas," *Adv. Phys.*, vol. 25, no. 5, pp. 517–553, 1976.
- [130] C. S. MacLatchy, "Langmuir probe measurements of ion density in an atmospheric-pressure air-propane flame," *Combust. Flame*, vol. 36, pp. 171–178, 1979.
- [131] R. M. Clements and P. R. Smy, "Electrostatic-Probe Studies in a Flame Plasma," *J. Appl. Phys.*, vol. 40, no. 11, pp. 4553–4558, Oct. 1969.
- [132] R. M. Clements and P. R. Smy, "Ion Current from a Collision-Dominated Flowing Plasma to a Cylindrical Electrode Surrounded by a Thin Sheath," *J. Appl. Phys.*, vol. 41, no. 9, pp. 3745–3749, Aug. 1970.
- [133] C. H. Su and R. E. Kiel, "Continuum Theory of Electrostatic Probes," *J. Appl. Phys.*, vol. 37, no. 13, pp. 4907–4910, Dec. 1966.
- [134] P. R. Smy and A. I. Noor, "High-pressure Langmuir probe in a weak flowing plasma or a plasma sheath," *J. Appl. Phys.*, vol. 47, no. 4, pp. 1327–1331, Apr. 1976.
- [135] T. L. Labus and E. P. Symons, "Experimental investigation of an axisymmetric free jet with an initially uniform velocity profile," 1972.
- [136] E. C. B. B. Aragão, J. C. Nascimento, A. D. Fernandes, F. T. F. Barbosa, D. C. Sousa, C. Oliveira, G. J. P. Abreu, V. W. Ribas, and B. N. Sismanoglu, "Low

Temperature Microplasma Jet at Atmospheric Pressure for Inducing Surface Modification on Polyethylene Substrates,” *Am. J. Condens. Matter Phys.*, vol. 4, no. 3A, pp. 1–7, Jun. 2014.

- [137] H. T. Schlichting and K. Gersten, *Boundary Layer theory*. New York: Springer-Verlag, 2000.